Geochemistry, Geophysics, Geosystems

RESEARCH ARTICLE
10.1029/2020GC009159

**Key Points:**
- We develop models of olivine texture evolution within deforming asthenosphere, and the associated directional variations in viscosity
- The effective viscosity of textured olivine can vary by an order of magnitude, depending on which slip system dominates the deformation
- Anisotropic viscosity promotes faster plate motion and ridge-parallel subduction initiation but impedes directional changes in plate motion

**Supporting Information:**
- Supporting Information S1

**Correspondence to:**
Á. Király,
agnes.kiraly@geo.uio.no

**Citation:**
Király, Á., Conrad, C. P., & Hansen, L. N. (2020). Evolving viscous anisotropy in the upper mantle and its geodynamic implications. *Geochemistry, Geophysics, Geosystems*, *21*, e2020GC009159. https://doi.org/10.1029/2020GC009159

Received 7 MAY 2020
Accepted 23 AUG 2020
Accepted article online 25 AUG 2020

# Evolving Viscous Anisotropy in the Upper Mantle and Its Geodynamic Implications

**Á. Király[1], C. P. Conrad[1], and L. N. Hansen[2]**

[1]Centre for Earth Evolution and Dynamics, University of Oslo, Oslo, Norway, [2]Department of Earth and Environmental Sciences, University of Minnesota, Minneapolis, MN, USA

**Abstract** Asthenospheric shear causes some minerals, particularly olivine, to develop anisotropic textures that can be detected seismically. In laboratory experiments, these textures are also associated with anisotropic viscous behavior, which should be important for geodynamic processes. To examine the role of anisotropic viscosity for asthenospheric deformation, we developed a numerical model of coupled anisotropic texture development and anisotropic viscosity, both calibrated with laboratory measurements of olivine aggregates. This model characterizes the time-dependent coupling between large-scale formation of lattice-preferred orientation (i.e., texture) and changes in asthenospheric viscosity for a series of simple deformation paths that represent upper mantle geodynamic processes. We find that texture development beneath a moving surface plate tends to align the *a* axes of olivine into the plate motion direction, which weakens the effective viscosity in this direction and increases plate velocity for a given driving force. Our models indicate that the effective viscosity increases for shear in the horizontal direction perpendicular to the *a* axes. This increase should slow plate motions and new texture development in this perpendicular direction and could impede changes to the plate motion direction for tens of millions of years. However, the same well-developed asthenospheric texture may foster subduction initiation perpendicular to the plate motion and deformations related to transform faults, as shearing on vertical planes seems to be favored across a sublithospheric olivine texture. These end-member cases examining shear deformation in the presence of a well-formed asthenospheric texture illustrate the importance of the mean olivine orientation, and its associated viscous anisotropy, for a variety of geodynamic processes.

**Plain Language Summary** The uppermost layer of Earth's mantle, the asthenosphere, experiences large deformations due to a variety of tectonic processes. During deformation, grains of olivine, the main rock-forming mineral in the asthenosphere, rotate into a preferred direction parallel to the deformation, developing a texture that can affect the response of the asthenosphere to tectonic stresses. Laboratory measurements show that the deformation rate depends on the orientation of the shear stress relative to the olivine texture. We use numerical models to apply the findings of the laboratory measurements to geodynamic situations that are difficult to simulate in a laboratory. These models track the development of olivine texture and its directional response to shear stress, which are highly coupled. Our results suggest that anisotropic viscosity in the asthenosphere can significantly affect the motions of tectonic plates, as plate motion in a continuous direction should become faster, while abrupt changes in the direction of plate motion should meet high resistance in the underlying asthenosphere. We suggest that olivine textures in the asthenosphere play a critical role in upper mantle dynamics.

## 1. Introduction

The physical characteristics of the upper mantle, for example, its density and rheology, control a variety of surface features, such as general tectonic regime, faulting characteristics, dynamic topography, and plate velocity. Many of these features are thus related to the properties of olivine, which comprises ~60% of the upper mantle (Stixrude & Lithgow-Bertelloni, 2005). It has long been known that olivine is anisotropic in its elastic properties, and this directional dependence has been observed in the upper mantle using seismic waves (e.g., Tanimoto & Anderson, 1984). This observed seismic anisotropy is mainly the result of the lattice preferred orientation (LPO, or texture) of the olivine crystals, which causes the speed of seismic waves to depend on propagation direction and additionally causes shear waves to split into two perpendicularly polarized waves (faster and slower) (Bamford & Crampin, 1977; Christensen, 1984; Mainprice et al., 2015). The texture (or LPO) itself is thought to result from shear strain in the upper mantle, which causes olivine crystals to rotate into a preferred direction, generally with the seismically fast axis parallel to the direction of shearing (e.g., Ribe, 1989; Karato & Wu, 1993). Seismic observations of this anisotropy have been used to infer patterns of upper mantle deformation (Long & Becker, 2010), for example, related to tectonic plate motions (e.g., Becker, 2008; Becker et al., 2003; Becker et al., 2014, 2008; Behn et al., 2004; Conrad & Behn, 2010; Gaboret et al., 2003), subduction (e.g., Long, 2013), continental collision (e.g., Silver, 1996), and motion on transform faults (e.g., Eakin et al., 2018).

Early laboratory experiments found that olivine anisotropy is not limited to its elastic properties, but olivine also exhibits anisotropy in its viscous behavior. Durham and Goetze (1977) demonstrated that the deformation rate of a single olivine crystal is orientation dependent and can vary by a factor of 50. To assess the role of single-crystal anisotropy in controlling the anisotropy of an aggregate of crystals, Hansen et al. (2012) first deformed aggregates of olivine in torsion and subsequently deformed them in extension. In torsion, the samples gradually weaken as the texture forms, but subsequent extensional deformation normal to the initial shear plane is characterized by a factor of 14 increase in viscosity. Similarly, but in a reverse order, Hansen, Warren, et al. (2016) first deformed aggregates of olivine in extension and subsequently deformed them in torsion. In extension, the samples gradually weaken as the texture forms, but subsequent torsional deformation is again characterized by much higher viscosities. Taken together, these experiments demonstrate that prolonged deformation in a consistent orientation leads to texture formation that reduces the viscosity, and a subsequent change in the orientation of deformation results in a dramatic increase in the viscosity.

However, Hansen, Warren, et al.'s (2016) laboratory experiments were only able to test a small number of deformation paths (i.e., first extension, then torsion, and vice versa), making it difficult to directly apply their results to deformation in the mantle. To apply their results more generally to mantle deformation, Hansen, Conrad, et al. (2016) used the existing experiments to define and calibrate a mechanical model of slip system activities and texture development within olivine aggregates. This model can predict both the evolution of olivine textures and the associated anisotropic viscous behavior for olivine aggregates undergoing arbitrary deformation paths. This coupled micromechanical and textural development model enables us to investigate the role of viscous anisotropy for a range of geodynamic processes.

Decades ago, researchers used early numerical modeling techniques to test the relevance of viscous anisotropy on geodynamical processes, such as mantle convection or postglacial rebound (Christensen, 1987). These studies relied on the laboratory measurements of Durham and Goetze (1977), which constrained the anisotropic behavior of single olivine crystals, and the work of Karato (1987), who studied the mechanisms of olivine texture formation. Due to the absence of more detailed laboratory data, previous modelers assumed transverse isotropy in a two-dimensional mantle (i.e., isotropic viscosity for shearing in the horizontal plane and anisotropy expressed as differences between shearing in the horizontal and vertical directions). More recently, the effect of anisotropic viscosity on mantle convection has been revisited (Mühlhaus et al., 2003), with additional investigations into Raleigh-Taylor instabilities and subduction zone processes within an anisotropically viscous mantle and/or lithosphere (Lev & Hager, 2008; 2011). These studies are based on the director method (Mühlhaus et al., 2002), which models olivine orientations as a set of directors, that is, 2-D unit vectors pointing normal to the easy shear plane. Anisotropic viscosity is expressed by a combination of normal and shear viscosities, and the effective shear viscosity is a function of the distribution of the directors. Furthermore, because the directors are advected and rotated by the flow, this method effectively couples texture development to the anisotropic viscosity of the mantle. The 2-D nature of the director method, however, limits its ability to capture the complete anisotropy associated with olivine, which has three independent slip systems that accommodate deformation at different rates (Hansen, Conrad, et al., 2016).

Here we have modified the director method to accommodate three-dimensional deformations of olivine aggregates using the micromechanical approach of Hansen, Conrad, et al. (2016). This model is calibrated by laboratory constraints on slip system activities and parameters of texture development (i.e., the relative rotation rates of the different olivine slip systems, see Table 1 in Hansen, Conrad, et al., 2016. The resulting model allows us to explore both the texture development of an olivine aggregate in a wide range of deformation paths and the mechanical response of these textured aggregates to applied stresses associated with these deformation paths. Our goal is to create first-order models of tectonic plate movement subject to a continuous driving force (e.g., slab pull) in one direction. As the olivine texture develops in the asthenosphere, we expect the mechanical response of the system to change as a function of time and accumulated strain, resulting in a changing plate velocity. Next, by changing the direction of the driving force, we can examine the response of the system to the application of stress in a new direction. The resulting deformation paths are analogs for geodynamic applications such as changes in the direction of plate movement, lithospheric dripping, initiation of subduction, and transform faulting. These simple exercises lead us to a better understanding of the interplay among olivine texture development, anisotropic mantle rheology, and large-scale geodynamic processes.

## 2. Methods

### 2.1. Mathematical Formulation

Our method is based on the micromechanical model described and characterized by Hansen, Conrad, et al. (2016). This approach uses a pseudo-Taylor approximation (after Taylor, 1938) to calculate the stress needed to create an equivalent strain rate on each olivine crystal, allowing for slip along three linearly independent slip systems. Each slip system is characterized by a critical shear stress that describes its strength relative to the isotropic strength of the aggregate. The best fit model parameters obtained by Hansen, Conrad, et al. (2016) for the pseudo-Taylor model are the following: 0.30 for the (010)[100] slip system, 0.27 for the (001)[100] slip system, and 1.29 for the (010)[001] slip system. The micromechanical model is coupled to a texture development model, in which the deformation of the olivine aggregate results in grain rotations. The rotation rate depends on the orientation of each grain with respect to the deformation, and a set of texture parameters that define the relative rotation rates along the four olivine slip systems (see Table 1 in Hansen, Conrad, et al., 2016). These combined models provide the basis for a method to calculate the anisotropic viscosity (or conversely the fluidity) for any given olivine texture. The resulting three-dimensional tensor can then be used to predict the deformation behavior for several geodynamic applications. In the following, we present details of this method and the results of first-order models in which the olivine-rich upper mantle undergoes different deformation paths induced by temporal variations in an applied shear stress.

To calculate the strain rate induced by the imposed stress, some further steps are necessary beyond those described by the mechanical model of Hansen, Conrad, et al. (2016). The macroscopic constitutive relationship between stress and strain rate for an anisotropic viscous medium is

$$\sigma_{kl} = \eta_{ijkl}\dot{\varepsilon}_{ij}, \tag{1}$$

where $\dot{\varepsilon}_{ij} = \frac{1}{2}\left(\frac{\partial v_i}{\partial x_j} + \frac{\partial v_j}{\partial x_i}\right)$ is the strain rate tensor, $\sigma_{kl}$ is the deviatoric stress tensor, and $\eta_{ijkl}$ is the viscosity tensor (Christensen, 1987; Pouilloux et al., 2007). Due to their symmetry, the deviatoric stress and the strain rate tensors can both be reduced to vectors using Kelvin notation, which preserves the norm of each of the tensors in (1) (Dellinger et al., 1998),

$$\dot{\varepsilon}_{ij} = \begin{bmatrix} \dot{\varepsilon}_{11} & \dot{\varepsilon}_{12} & \dot{\varepsilon}_{13} \\ \dot{\varepsilon}_{12} & \dot{\varepsilon}_{22} & \dot{\varepsilon}_{23} \\ \dot{\varepsilon}_{13} & \dot{\varepsilon}_{23} & \dot{\varepsilon}_{33} \end{bmatrix} \equiv \begin{bmatrix} \dot{\varepsilon}_{11} \\ \dot{\varepsilon}_{22} \\ \dot{\varepsilon}_{33} \\ \sqrt{2}\dot{\varepsilon}_{23} \\ \sqrt{2}\dot{\varepsilon}_{13} \\ \sqrt{2}\dot{\varepsilon}_{12} \end{bmatrix} \equiv \begin{bmatrix} \dot{\varepsilon}_{1} \\ \dot{\varepsilon}_{2} \\ \dot{\varepsilon}_{3} \\ \dot{\varepsilon}_{4} \\ \dot{\varepsilon}_{5} \\ \dot{\varepsilon}_{6} \end{bmatrix} \tag{2}$$

$$\sigma_{ij} = \begin{bmatrix} \sigma_{11} & \sigma_{12} & \sigma_{13} \\ \sigma_{12} & \sigma_{22} & \sigma_{23} \\ \sigma_{13} & \sigma_{23} & \sigma_{33} \end{bmatrix} \equiv \begin{bmatrix} \sigma_{11} \\ \sigma_{22} \\ \sigma_{33} \\ \sqrt{2}\sigma_{23} \\ \sqrt{2}\sigma_{13} \\ \sqrt{2}\sigma_{12} \end{bmatrix} \equiv \begin{bmatrix} \sigma_{1} \\ \sigma_{2} \\ \sigma_{3} \\ \sigma_{4} \\ \sigma_{5} \\ \sigma_{6} \end{bmatrix}. \tag{3}$$

It follows that the viscosity can be reduced to a 6 × 6 tensor (e.g., Pouilloux et al., 2007). Because of the nonlinear rheological behavior of olivine, the viscosity tensor is also a function of stress. The rheology can thus be expressed by a stress-independent material constant ($\underline{\underline{A}}$), which relates to the viscosity, as

$$\mathrm{inv}\left(\eta_{ij}\right) = A_{ij} \cdot {II_\sigma}^{(n-1)/2}. \tag{4}$$

Equation 4 describes the fluidity of the material at a given stress, where $II_\sigma$ denotes the second invariant of the deviatoric stress and $n$ is the power law factor. Using Equation 4, the strain rate can be expressed as a function of the stress and the fluidity according to

$$\begin{bmatrix} \dot{\varepsilon}_1 \\ \dot{\varepsilon}_2 \\ \dot{\varepsilon}_3 \\ \dot{\varepsilon}_4 \\ \dot{\varepsilon}_5 \\ \dot{\varepsilon}_6 \end{bmatrix} = \begin{bmatrix} A_{11} & A_{12} \\ A_{21} & A_{22} \\ & A_{31} \\ & A_{41} \\ & A_{51} \\ & A_{61} \end{bmatrix} \cdot \begin{bmatrix} \sigma_1 \\ \sigma_2 \\ \sigma_3 \\ \sigma_4 \\ \sigma_5 \\ \sigma_6 \end{bmatrix} \cdot {II_\sigma}^{(n-1)/2}. \tag{5}$$

To solve Equation 5 for the strain rate, the material constant $\underline{\underline{A}}$, which we will refer to as the fluidity parameter tensor, must be known. $\underline{\underline{A}}$ is a function of temperature and grain size and also depends on the crystal orientations of the aggregate. The micromechanical model of Hansen, Conrad, et al. (2016) allows us to find the stress needed to produce any strain rate for a given olivine texture. Therefore, to find the components of $\underline{\underline{A}}$ with the pseudo-Taylor mechanical model, we need to apply six different strain rates to the aggregate and calculate the six stress vectors that are required to produce these strain rates. The six strain rates define the columns of the tensor $\underline{\underline{E}}$,

$$\underline{\underline{E}} = \begin{bmatrix} \dot{\varepsilon}_0 & -\dot{\varepsilon}_0/2 & -\dot{\varepsilon}_0/2 & 0 & 0 & 0 \\ -\dot{\varepsilon}_0/2 & \dot{\varepsilon}_0 & -\dot{\varepsilon}_0/2 & 0 & 0 & 0 \\ -\dot{\varepsilon}_0/2 & -\dot{\varepsilon}_0/2 & \dot{\varepsilon}_0 & 0 & 0 & 0 \\ 0 & 0 & 0 & \dot{\varepsilon}_0/\sqrt{2} & 0 & 0 \\ 0 & 0 & 0 & 0 & \dot{\varepsilon}_0/\sqrt{2} & 0 \\ 0 & 0 & 0 & 0 & 0 & \dot{\varepsilon}_0/\sqrt{2} \end{bmatrix}, \tag{6}$$

where $\dot{\varepsilon}_0$ is the applied strain rate amplitude. By applying the micromechanical model of Hansen, Conrad, et al. (2016) separately to each column of $\underline{\underline{E}}$, we can compute the set of stress tensors associated with each of these six strain rates. We use these stress tensors to construct the tensor $\underline{\underline{S}}$, for which each row represents the stress vector associated with the strain rate vector in each column of $\underline{\underline{E}}$, multiplied by ${II_\sigma}^{(n-1)/2}$. These two tensors are related according to the equation

$$\underline{\underline{E}} = \underline{\underline{A}} \cdot \underline{\underline{S}}, \tag{7}$$

where $\underline{\underline{S}} =$

$$\begin{bmatrix} {II_{\sigma_1}}^{(n-1)/2}\sigma_{1_1} & {II_{\sigma_1}}^{(n-1)/2}\sigma_{2_1} & {II_{\sigma_1}}^{(n-1)/2}\sigma_{3_1} & {II_{\sigma_1}}^{(n-1)/2}\sigma_{4_1} & {II_{\sigma_1}}^{(n-1)/2}\sigma_{5_1} & {II_{\sigma_1}}^{(n-1)/2}\sigma_{6_1} \\ {II_{\sigma_2}}^{(n-1)/2}\sigma_{1_2} & {II_{\sigma_2}}^{(n-1)/2}\sigma_{2_2} & {II_{\sigma_2}}^{(n-1)/2}\sigma_{3_2} & {II_{\sigma_2}}^{(n-1)/2}\sigma_{4_2} & {II_{\sigma_2}}^{(n-1)/2}\sigma_{5_2} & {II_{\sigma_2}}^{(n-1)/2}\sigma_{6_2} \\ {II_{\sigma_3}}^{(n-1)/2}\sigma_{1_3} & {II_{\sigma_3}}^{(n-1)/2}\sigma_{2_3} & {II_{\sigma_3}}^{(n-1)/2}\sigma_{3_3} & {II_{\sigma_3}}^{(n-1)/2}\sigma_{4_3} & {II_{\sigma_3}}^{(n-1)/2}\sigma_{5_3} & {II_{\sigma_3}}^{(n-1)/2}\sigma_{6_3} \\ {II_{\sigma_4}}^{(n-1)/2}\sigma_{1_4} & {II_{\sigma_4}}^{(n-1)/2}\sigma_{2_4} & {II_{\sigma_4}}^{(n-1)/2}\sigma_{3_4} & {II_{\sigma_4}}^{(n-1)/2}\sigma_{4_4} & {II_{\sigma_4}}^{(n-1)/2}\sigma_{5_4} & {II_{\sigma_4}}^{(n-1)/2}\sigma_{6_4} \\ {II_{\sigma_5}}^{(n-1)/2}\sigma_{1_5} & {II_{\sigma_5}}^{(n-1)/2}\sigma_{2_5} & {II_{\sigma_5}}^{(n-1)/2}\sigma_{3_5} & {II_{\sigma_5}}^{(n-1)/2}\sigma_{4_5} & {II_{\sigma_5}}^{(n-1)/2}\sigma_{5_5} & {II_{\sigma_5}}^{(n-1)/2}\sigma_{6_5} \\ {II_{\sigma_6}}^{(n-1)/2}\sigma_{1_6} & {II_{\sigma_6}}^{(n-1)/2}\sigma_{2_6} & {II_{\sigma_6}}^{(n-1)/2}\sigma_{3_6} & {II_{\sigma_6}}^{(n-1)/2}\sigma_{4_6} & {II_{\sigma_6}}^{(n-1)/2}\sigma_{5_6} & {II_{\sigma_6}}^{(n-1)/2}\sigma_{6_6} \end{bmatrix}$$

In $\underline{\underline{S}}, \sigma_{i_j}$ denotes the $i$th component of the deviatoric stress in Kelvin notation corresponding to the $j$th column of $\underline{\underline{E}}$, calculated with the pseudo-Taylor method described by (Hansen, Conrad, et al., 2016), and $II_{\sigma_j}$ is the

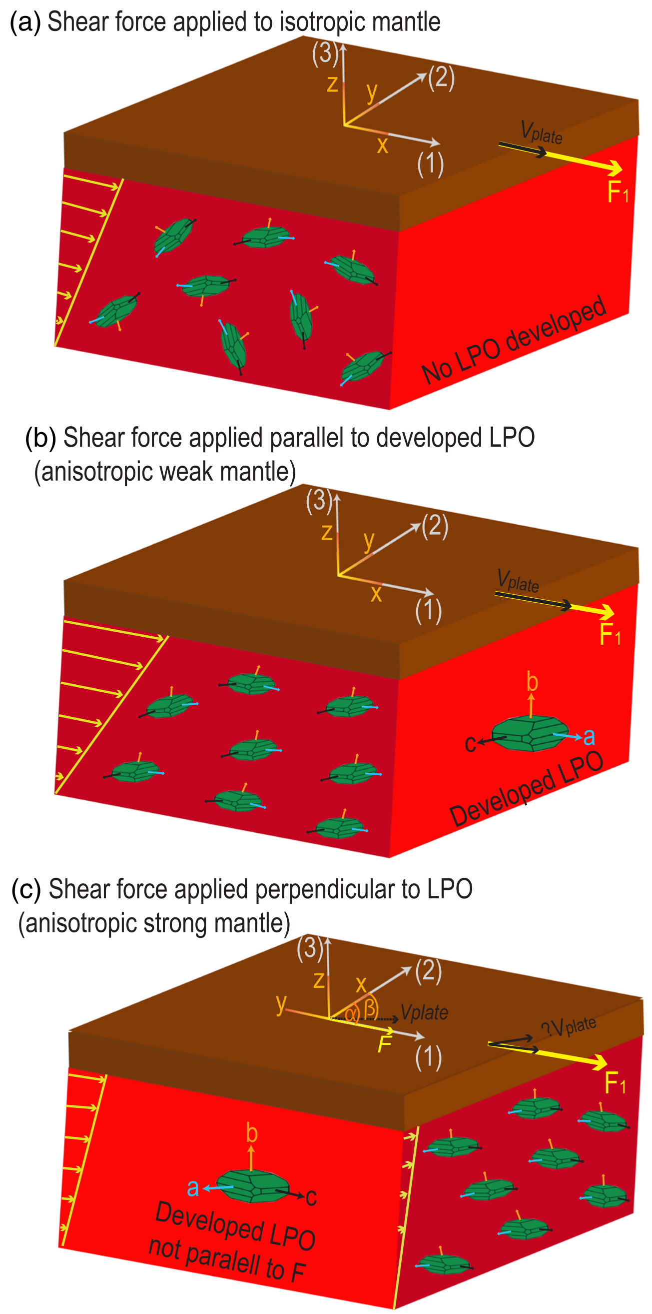


**Figure 1.** Relationship between anisotropic viscosity and olivine texture formation. (a) A force ($F_1$) applied to an initially isotropic asthenosphere (i.e., without a preexisting texture) yields a moderate plate speed, and the associated asthenospheric deformation fosters olivine texture development. (b) The same force applied parallel to the average *a*-axis orientation of a well-developed texture results in a much larger plate speed. (c) Applying this force parallel to the average *c*-axis orientation causes the plate to move much more slowly. The configuration depicted in panel (b) can evolve into the configuration depicted in panel (c) in two ways. Either the force can be rotated relative to the texture (as for many geodynamic scenarios) or the texture can be rotated with respect to the force (as illustrated in (c) and implemented in our modeling effort).

second invariant of each stress tensor (corresponding to the *j*th column of $\underline{\underline{E}}$). Equation 7 needs to be inverted to determine $\underline{\underline{A}}$. However, due to the incompressibility criteria and because $\underline{\underline{S}}$ builds up by deviatoric stresses, $\sum_{i=1}^{3} E_{ij} = 0 \wedge \sum_{i=1}^{3} S_{ij} = 0$ for each *j*. This means that $\underline{\underline{S}}$ is not invertible in its full form. However, we do not lose information by reducing both $\underline{\underline{E}}$ and $\underline{\underline{S}}$ by one column and one row (the first column and row) because the first component of both the strain rate and the deviatoric stress can be reconstructed from their second and third components. This reduction yields $\underline{\underline{E}}' = \underline{\underline{A}}' \cdot \underline{\underline{S}}'$, where each matrix has five rows and columns and a rank of 5. Hence, $\underline{\underline{S}}'$ is invertible, so

$$\underline{\underline{A}}' = \underline{\underline{E}}' \cdot \underline{\underline{S}}'\text{-1} \tag{8}$$

can be solved.

Knowing the fluidity parameter tensor, $\underline{\underline{A}}'$, for a given olivine texture allows us to compute the full strain rate tensor for any given applied stress tensor. The actual deformation that is produced depends on model assumptions about how this deformation is geodynamically expressed in the rock. In this study, we examine geodynamic processes associated with simple shear of the asthenosphere, for example, as produced by the motion of a surface plate over an asthenospheric layer (Figure 1). To implement this deformation, we impose a deformation gradient consistent with simple shear, for which the deformation tensor ($D_{ij}{=}\partial u_i/\partial x_j$) is

$$\underline{\underline{D_{F_1}}} = \begin{bmatrix} 0 & 2\dot{\varepsilon}_{12} & 2\dot{\varepsilon}_{13} \\ 0 & 0 & 2\dot{\varepsilon}_{23} \\ 0 & 0 & 0 \end{bmatrix} \tag{9}$$

for the case in which the asthenosphere is sheared with force $F_1$ (Figure 1) and thus driven by a stress $\sigma_{13}$. The deformation that results is described in (Equation 9) by $D_{12}$, $D_{23}$, and $D_{13}$, where $D_{12}$ and $D_{23}$ are only excited because of the anisotropic nature of the rheology. Note that we neglect the normal strain rate components ($D_{11} = D_{22} = D_{33} = 0$) assuming that the geometric constraints on the system do not permit net elongation or contraction in any direction. From the imposed deformation, we can calculate the associated texture evolution as a function of time for a given applied stress history. The time step in the calculation is set based on the strain rate to have 0.1 strain increment for each time step, which we have found to produce stable results.

### 2.2. Geodynamic Model

To investigate the influence of anisotropic viscous behavior in geodynamic scenarios with changing orientations of stress, we model the deformation of a set of olivine grains representing the behavior of the asthenosphere. We apply a shear stress (= force/area) of 0.68 MPa, which roughly corresponds to the shear stress acting on a plate of area 6,000 by 6,000 km that is necessary to balance an edge force of $4.1 \times 10^{12}$ N/m (a lower bound estimate for the value of slab pull force transferred to the plate from the negative buoyancy of a subducting oceanic lithosphere; Schellart, 2004) above a 200 km thick asthenosphere (Figure 1a). We track the deformation of the asthenosphere using the micromechanical model of texture development and viscous anisotropy described above. Based on the anisotropic properties of a representative olivine aggregate, we compute the strain rate within the asthenosphere, and associated parameters such as plate speed and movement direction, all as a function of time, accumulated strain, and olivine texture development. To calculate the plate velocity, we assume that the velocity is 0 at the base of the $H_a = 200$ km thick asthenosphere and that the horizontal velocity at the top of the asthenosphere is the plate velocity. Hence,

$$V_{\mathrm{plate}} = 2\sqrt{\dot{\varepsilon}_{13}^2 + \dot{\varepsilon}_{23}^2}H_{\mathrm{a}}. \tag{10}$$

To investigate different deformation paths that are analogs for a variety of upper mantle processes, we change the orientation of the applied shear stress, and consequently the deformation applied to the asthenosphere, at a chosen instant after an olivine texture has formed (Figure 1b). Such a change could be induced by a change in the external driving forces applied to the asthenosphere. An intuitively simple approach would be to rotate the imposed driving stress relative to the texture that initially formed. However, for numerical and analytical simplicity, we instead rotate the olivine texture with respect to the imposed stress (as shown in Figure 1c), which is held steady. This approach produces an equivalent result and allows us to keep the definition of both the shear stress and the deformation tensors (Equation 9) unchanged. Later, we will discuss the geodynamic scenarios represented by the various rotations of the olive texture with respect to the applied shear stress.

We define the angles $\alpha$ and $\beta$ as the orientations of the imposed shear stress and the resulting plate motion with respect to a coordinate system fixed in the asthenosphere ($x$ axis, Figure 1c). Thus, $\alpha$ is the angle between the (1) axis (which is the same as the direction of the shear stress) and the $x$ axis (which is the angle of rotation of the texture) in Figure 1, and $\beta$ is the angle between the plate motion direction and the $x$ axis. The horizontal shear components of the strain rate ($\dot{\varepsilon}_{23} \wedge \dot{\varepsilon}_{13}$) are used to calculate the direction of the plate movement ($\beta$),

$$\beta = a\tan\left(\frac{\dot{\varepsilon}_{23}}{\dot{\varepsilon}_{13}}\right) + \alpha. \tag{11}$$

## 3. Results

We present the results of 27 models with different deformation paths. Each model result is an average of five individual runs, each initiated with 1,000 olivine grains with initial orientations randomly drawn from a uniform distribution. Therefore, we effectively represent the asthenosphere under a large (6,000 × 6,000 km$^2$) plate using the average of five model runs of 1,000 grains each.

### 3.1. Monotonic Simple Shear

First, we present the evolution of asthenospheric strain rates and olivine texture development from a uniformly distributed texture (i.e., an isotropic mantle) to a well-developed texture (anisotropic, weak mantle). As the mantle accumulates strain, the $a$ axes of olivine rotate toward the shear direction (Figure 1b), developing a texture that decreases the effective viscosity of the asthenosphere and, therefore, increases the velocity of the plate. We examined two sets of models differing only in the randomly created, uniformly distributed orientations at the start of the models (Figure 2, black and gray curves). The similarity of these two model averages implies that the average of model runs with 5 × 1,000 grains gives a reasonably stable result. However, subtle differences in the initial textures of the two models can still cause minor differences in the amplitudes of the fluidity parameters (Figure 2b).

The amplitude of the shear strain rate ($|\dot{\varepsilon}| = 2 \cdot \sqrt{\dot{\varepsilon}_{12}{}^2 + \dot{\varepsilon}_{13}{}^2 + \dot{\varepsilon}_{23}{}^2}$, simply referred to as strain rate hereafter) exhibits characteristic variations throughout this deformation (Figure 2), which result from the texture evolution of the olivine aggregates and the associated changes in the fluidity parameter tensor (Figures 2b and 2c). With an initially uniform olivine distribution, the strain rate in the asthenosphere is 1.5–1.7 × $10^{-14}$ $s^{-1}$, which corresponds to a plate velocity of ~9.5–10.5 cm/year velocity. As accumulated strain increases, the olivine texture develops, the effective viscosity of the asthenosphere decreases, and the plate velocity increases, reaching a maximum of 14.8 cm/year (2.4 × $10^{-14}$ $s^{-1}$) around a strain of 8, that is,

10.1029/2020GC009159

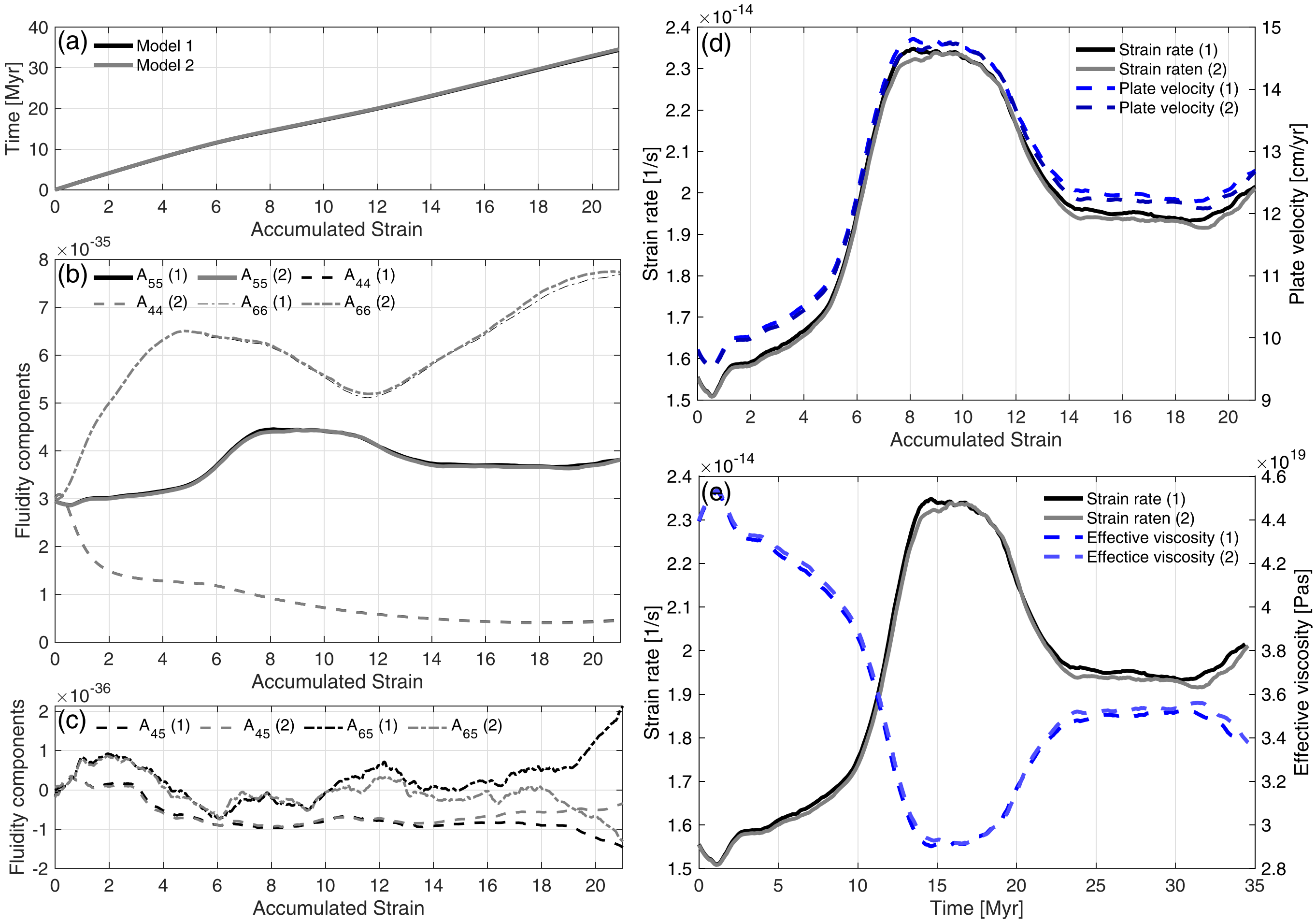


**Figure 2.** Results of two sets of models with constant shear stress ($\sigma_{13}$ = 0.68 MPa), both computed as average results from five model runs each starting from 1,000 uniformly distributed grain orientations. (a) Accumulated strain as a function of time. (b) Shear components of the fluidity parameter tensor. $A_{44}$ and $A_{66}$ are fictive curves since the associated stresses for these components, $\sigma_{23}$ and $\sigma_{12}$, are zero. $A_{55}$ represents the fluidity for the actual applied stress $\sigma_{13}$. (c) Fluidity components relating strain rates in the perpendicular direction ($A_{45}$) or plane ($A_{65}$) with respect to the shear stress ($\sigma_{13}$). (d) Strain rate ($|\dot{\varepsilon}|$) and plate velocity ($V_{\text{plate}}$) as a function of the accumulated strain. The plate velocity is calculated from the horizontal strain rate component (Equation 10), while the strain rate curve is the norm of the shear strain rate tensor (for which only the nondiagonal components are nonzero). (e) Strain rate and effective viscosity as a function of time instead of accumulated strain.

after ~14 Myr of shearing. With further shearing, the plate velocity decreases and subsequently stabilizes at 12.3 cm/year ($1.9 \times 10^{-14}$ 1/s). The effective viscosity is inversely proportional to the strain rate, reaching a minimum at ~14.5 Myr (strain of 8) and slightly increasing during the later history. The magnitude of the viscosity varies from 2.9 to $4.5 \times 10^{19}$ Pa·s. Hence, with continuous shearing, any further evolution of the olivine texture decreases the asthenosphere's effective viscosity by less than a factor of 2.

Both the shear components of the fluidity tensor ($A_{44}$, $A_{55}$, and $A_{66}$ in Figure 2b) and the off-diagonal components ($A_{45}$ and $A_{65}$ in Figure 2c) exhibit variations with time as the olivine texture develops. The nonzero component of the stress tensor is $\sigma_{13}$, ($\sigma_5$ in Kelvin notation), which means that $A_{55}$ represents the fluidity in the shear direction (shearing on the (3) plane in the (1) direction, creating $\partial v_1/\partial x_3$). Note that since $\sigma_{31} = \sigma_{13}$ (symmetry of the stress tensor), then $A_{55}$ also represents the fluidity for the reciprocal deformation (i.e., shearing on the (1) plane in the (3) direction, creating $\partial v_3/\partial x_1$). $A_{44}$ and $A_{66}$ represent the values of the fluidity that would control the deformation (shearing given by $\partial v_3/\partial x_2$ or $\partial v_2/\partial x_3$ for $A_{44}$ and by $\partial v_1/\partial x_2$ or $\partial v_2/\partial x_1$ for $A_{66}$) if we were to change the shear stress to $\sigma_{23}$ ($= \sigma_{32}$) or $\sigma_{12}$ ($= \sigma_{21}$), respectively.

Initially, there is no preferred orientation of the olivine grains, and the three shear fluidity components are the same. As the asthenosphere deforms and the texture develops in association with shearing on the (3) plane in the (1) direction, $A_{55}$ increases, which is associated with a decrease in viscosity and an increase in the plate velocity. In contrast, the fluidity component $A_{44}$ ($A_{2323}$) decreases, which indicates that it would become harder and harder to shear the asthenosphere with a stress $\sigma_{23}$, which would induce shearing on the (3) plane in the (2) direction (i.e., plate motion in a perpendicular direction), or reciprocally on the (2) plane in the (3) direction. Surprisingly, $A_{66}$ increases with progressive deformation, and most of the time it is even larger than $A_{55}$. Thus, as the texture develops, it also becomes easier to shear the asthenosphere along the vertical (2) plane in the (3) direction (or, reciprocally, along the (3) plane in the (2) direction). The $A_{45}$ and $A_{65}$ off-diagonal components (Figure 2c) are noteworthy because these components couple $\sigma_{13}$ to $\dot{\varepsilon}_{23}$ and $\dot{\varepsilon}_{12}$, respectively (Equation 5). These components are initially zero but do take on finite values with progressive deformation. In other words, as the anisotropy of the system develops, the applied shear stress begins to induce shear strains on planes other than the primary shear plane, and in directions other than the primary shear direction. However, because these components are 2 orders of magnitude lower than $A_{55}$, the strain rate in this simple case is dominated by the effects of $A_{55}$. Consequently, values of $A_{55}$ (Figure 2b), strain rate (Figures 2d and 2e), and plate velocity (Figures 2d) all exhibit the same trend as a function of time and strain.

#### 3.1.1. Rheology and Texture Parameters

As demonstrated above, the plate velocity (calculated from the horizontal strain rate) and the shear-parallel ($A_{55}$) component of the fluidity tensor are linearly dependent, and those terms are inversely proportional to the effective viscosity. To further understand the initially increasing and subsequently decreasing evolution of the strain rate, the relationship between the texture and the rheological behavior of the asthenosphere (olivine aggregate) needs to be examined. In the literature, a number of texture parameters have been proposed to quantify the orientation distribution of a group of crystals. For example, the *J* index (also referred to as the texture strength) provides a metric for the degree of alignment of crystal orientations (Bunge, 1982), varying between 1 (uniform distribution) and infinity (single-crystal texture). The *M* index (Skemer et al., 2005) also assesses the degree of alignment and results from the difference between the uncorrelated and the uniform misorientation angle distributions, with a value between 0 (uniform distribution) and 1 (single-crystal texture). We calculated both the *J* and the *M* indices with MTEX (Mainprice et al., 2015) and plotted the latter along with the plate velocity against the accumulated strain (Figure 3a). Comparing the two curves (blue and yellow, for the plate velocity and the *M* index, respectively), no direct relationship is observable.

We examine the subtleties of the textural development with pole figures that indicate the orientation distributions of the three main axes of the olivine grains (Figure 3). These plots illustrate that better correlation may be found between the plate velocity and the distributions of individual axes instead of the *M* index, which describes the orientation distribution of all three axes. For example, as the plate velocity decreases between the strains of 8 and 16, the distributions of the *a* and *c* axes become more girdled, while the distribution of the *b* axes becomes more clustered, resulting in an increasing *M* index. Thus, the qualitative comparison of the pole figures with the plate velocity suggests that the distribution of *a* axes, which represents the easiest slip direction, exerts a primary influence on the rheological behavior of the aggregate.

Therefore, we calculate three additional parameters that describe the degree to which the orientation distribution is random (*R*), girdle like (*G*), or point like (*P*), for each crystallographic axis (*a* axes: *P-a*, *G-a*, *R-a*; *b* axes: *P-b*, *G-b*, *R-b*; and *c* axes: *P-c*, *G-c*, *R-c*) (Vollmer, 1990). All three parameters vary between 0 and 1, and the sum of all three parameters is 1 for each axis distribution. We plot these texture parameters against the accumulated strain and the plate velocity (Figure 3a), revealing some correlation between the *P-a* values and the plate velocity and some anticorrelation between the *G-a* values and the plate velocity.

### 3.2. Change in the Direction of the Shear Force

The aim of this section is to test several deformation paths that, to first order, represent those expected for different geodynamic processes. For example, changing the force acting on the plate from the (1) direction to the (2) direction (i.e., from force $F_1$ to force $F_2$ in Figure 4) represents a change in the direction of the pull force acting on a tectonic plate and should change the direction of plate movement (Figure 4). Other changes

10.1029/2020GC009159

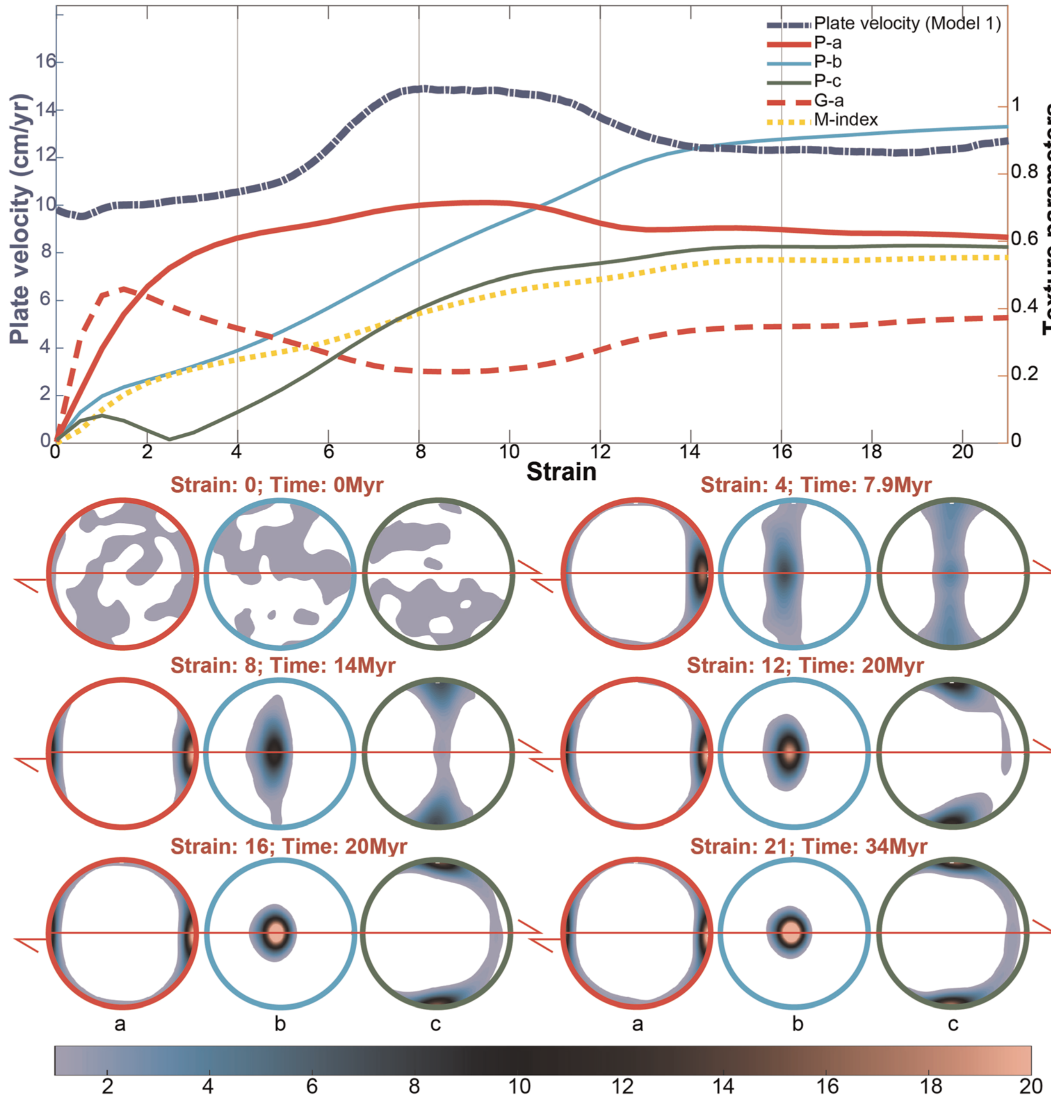


**Figure 3.** The evolution of plate velocity and several texture parameters as a function of (top) accumulated strain with (bottom) pole figures indicating the orientation density of *a*, *b*, and *c* axes for olivine aggregates with different total strains. The color scale indicates multiples of a uniform density. The shear direction (marked by red arrows) is toward the right, and the shear plane is the same as the plae of the figure.

to the force that we explore are illustrated in Figure 4. These force directions can mimic shearing induced by subduction initiation and/or dripping ($F_3$ and $F_5$) or the start of transform faulting ($F_4$ and $F_6$).

First, we describe the results of an instantaneous change in the direction of the asthenospheric shear force (from $F_1$ to $F_2$, $F_3$, $F_4$, $F_5$, or $F_6$ in Figure 4). We then examine the influence on the deformation behavior of 1) the rate of rotation of the shear force direction (from 1 to 12 Myr/90°), 2) the amount of texture development prior to the change, and 3) the total rotation angle of the driving stress when switching from $F_1$ to $F_2$. As noted above, we implement a change in the driving force (or shear stress) by rotating the textured olivine aggregate (formed by applying the shear of model 1 for a chosen amount of accumulated strain) while keeping the shear stress constant (Figure 1c).

### 3.2.1. Instantaneous Change in Shear Direction

At a strain of 8 (i.e., after shearing the olivine aggregate for 14.5 Myr), the *a* axes distribution reaches the maximum value of *P* (Figure 3). Hence, to maximize the effect of anisotropy in our tests, we first reach a shear strain of 8 by applying $\sigma_{13}$ with deformation consistent with applying the force $F_1$ (using the same initial texture as in model 1) and then switching to a new force direction (defined in Figure 4). Due to the

10.1029/2020GC009159

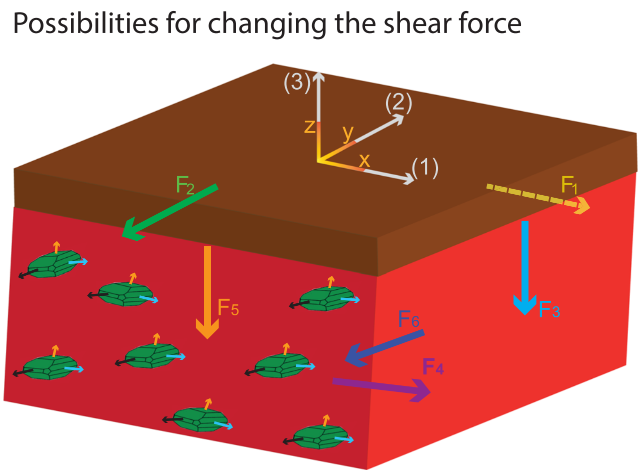


**Figure 4.** Possible orientations for the shear force, with $F_1$ representing the orientation associated with initial plate motion (e.g., as in Figure 1b). $F_2$ represents a shear force acting on a horizontal plane at 90° to the initial plate motion direction, analogous to a change in the direction of the plate driving force. $F_4$ and $F_6$ represent forces that create shearing deformation in a horizontal direction along vertical planes, analogous to transform shear zones. $F_3$ and $F_5$ represent forces that create shearing deformation in a vertical direction on vertical planes, analogous to subduction initiation or a dripping instability. In our analysis, all forces have the same magnitude as $F_1$.

symmetric nature of the stress tensor, $F_3$ is achieved using the same applied stress as $F_1$, but by employing different applied boundary conditions that enforce deformation consistent with vertical shearing, that is, $\underline{\underline{D_{F_3}}} = \begin{bmatrix} 0 & 0 & 0 \\ 2\dot{\varepsilon}_{12} & 0 & 0 \\ 2\dot{\varepsilon}_{13} & 2\dot{\varepsilon}_{23} & 0 \end{bmatrix} = \underline{\underline{D_{F_1}}}^T$. $F_2$ and $F_5$ are consistent with a stress tensor in which only $\sigma_{23}$ and $\sigma_{32}$ are nonzero and deformation is given by $\underline{\underline{D_{F_2}}} = \begin{bmatrix} 0 & 0 & 2\dot{\varepsilon}_{13} \\ 2\dot{\varepsilon}_{12} & 0 & 2\dot{\varepsilon}_{23} \\ 0 & 0 & 0 \end{bmatrix} \wedge \underline{\underline{D_{F_5}}} = \underline{\underline{D_{F_2}}}^T$. $F_4$ and $F_6$ are both consistent with a stress tensor where only $\sigma_{12}$ and $\sigma_{21}$ are nonzero and induce deformation given by $\underline{\underline{D_{F_4}}} = \begin{bmatrix} 0 & 2\dot{\varepsilon}_{12} & 2\dot{\varepsilon}_{13} \\ 0 & 0 & 0 \\ 0 & 2\dot{\varepsilon}_{23} & 0 \end{bmatrix} \wedge \underline{\underline{D_{F_6}}} = \underline{\underline{D_{F_4}}}^T$. As mentioned before, these deformations are equivalent to those achieved by rotating the mantle (i.e., the olivine aggregate) with respect to the force $F_1$ and keeping the imposed boundary conditions expressed by the deformation tensor $D_{F_1}$ (Equation 9). A 90° rotation of the aggregate around the $x$ axis represents a change from $F_1$ to $F_4$, around the $y$ axis reproduces $F_3$, and around the $z$ axis reproduces $F_2$. $F_5$ is modeled by rotating the aggregate around the $x$ and then $z$ axes, and $F_6$ is modeled by rotation around the $x$ then $y$ axes. Referring to Figure 4, rotating the aggregate around its $x$ or its $x$ then $y$ axes represents shearing produced by a transform fault ($F_4$ or $F_6$); rotation around the $y$ or the $x$ then $z$ axes represents shearing associated with dripping or subduction ($F_3$ or $F_5$), while rotation around the $z$ axis represents a change in the direction of the horizontal shear ($F_2$) (e.g., due to a change in the direction of slab pull force).

The effect of changing the shear direction largely depends on the direction of the new shear stress with respect to the textured mantle (Figure 5). For example, when the rotation results in a new shear stress that primarily induces deformation on the hardest (010)[001] slip system ($F_2$ or $F_5$), the strain rate decreases dramatically, from $2.3 \times 10^{-14}$ to $4.9 \times 10^{-15}$ s$^{-1}$ (Figure 5b, orange and green curves). Translating to plate velocity, this change implies a decrease from 14.8 to 3 cm/year.

Note that reciprocal pairs of shear deformations (i.e., $F_1$-$F_3$, $F_2$-$F_5$, and $F_4$-$F_6$) are associated with the same stress state (shear stress given by $\sigma_{13}$, $\sigma_{23}$, and $\sigma_{12}$, respectively) and initially activate the same slip systems because they are deforming the same initial texture. Thus, the effective viscosity, and the associated deformation rates, for each of these pairs is initially the same (as shown at a strain of 8 in Figures 5a–5c, respectively). However, because the rotation associated with these deformation pairs is different (because we employ different boundary conditions $\underline{\underline{D}}$), the textures for these pairs evolve differently (Figures 5, right column), and their strain rates diverge (Figures 5, left column).

#### 3.2.1.1. Representing Change in Plate Motion Direction

Rotating the olivine aggregate around its $z$ axis represents a relative change in the direction of the plate driving force. The result of a model with 90° instantaneous rotation (green curve in Figure 5b) exhibits a dramatic reduction in strain rate and a slow recovery of the olivine texture after the rotation. By the end of the model run (total shear strain of 21) the strain rate has increased to $1.3 \times 10^{-14}$ s$^{-1}$, which is still less than the strain rate for the initially isotropic aggregate. Because of the slow deformation associated with the diminished strain rate, this partial recovery took almost 50 Myr. Examination of the change in olivine texture directly after the rotation (at strain of 8.5, Figure 5) illustrates that the orientations are well organized but that the preferred orientation is perpendicular to the direction of shearing (Figure 5). When the strain rate finally starts to increase, the $a$ is distribution is more random or girdle like rather than point like, even at a total strain of 21. Regarding the fluidity tensor, when the texture is rotated, the $A_{55}$ component (which relates $\sigma_{13}$ to $\dot{\varepsilon}_{13}$) decreases, while both $A_{45}$ and $A_{65}$ exhibit a minor increase, leading to similar values for all three components.

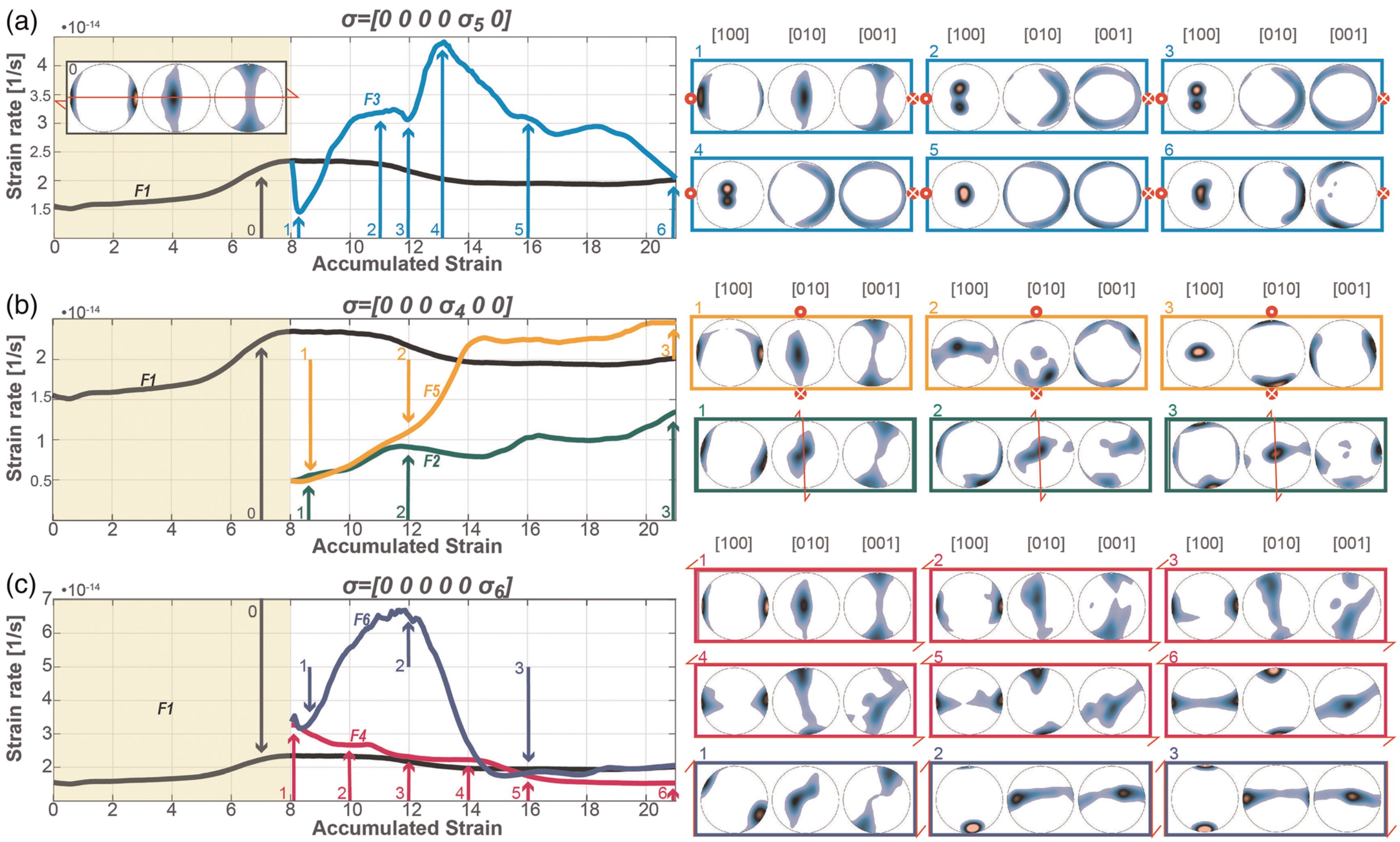


**Figure 5.** (a–c) Strain rate as a function of accumulated strain for the five different changes to the imposed shear force (Figure 4). On the left side, an initially isotropic aggregate is deformed with shear force $F_1$ until a strain of 8 (as in Figure 2d). At a strain of 8, the direction of the shear force is instantaneously changed to the directions $F_2$ through $F_6$ (Figure 4). Plots are grouped based on reciprocal pairs of deformation responding to the same imposed stress (see text). On the right side, pole figures indicate the texture for several points in the evolution denoted by arrows in the left diagrams. Note that all of the textures are presented relative to the mantle reference frame, and the shear force acting on the mantle is marked by red arrows (and arrow points and tails).

#### 3.2.1.2. Shear Forces Associated With Transform Faults

There are two possibilities for creating shear stress in a horizontal direction along a vertical plane, which roughly approximates the stress state associated with a transform fault. The possible shear forces are $F_4$ or $F_6$ (Figure 4), which produce very different paths in the strain rate evolution (Figure 5c) if there is already a well-developed texture associated with deformation due to $F_1$. At the time of rotation (at a strain of 8), both models exhibit an elevated strain rate (to $3.3 \times 10^{-14}$ s$^{-1}$) compared to the earlier deformation (driven by $F_1$). The pink curve, representing the switch from $F_1$ to $F_4$, after the initial peak strain rate slowly decreases to ~$1.5 \times 10^{-14}$ s$^{-1}$. Switching from $F_1$ to $F_6$ is relatively easy, as the model exhibits increasing strain rate (up to ~$6.7 \times 10^{-14}$ s$^{-1}$) associated with the texture evolution after the rotation for an additional shear strain of ~4 (Figure 5c, dark blue curve). This peak is followed by a quickly decreasing strain rate that stabilizes around ~$2 \times 10^{-14}$ s$^{-1}$, which is comparable to the strain rate for larger strains in reference model 1 (black curve). The high strain rate produced by the model representing $F_6$ is associated with a quick texture evolution and a point-like distribution in the new shear direction that is more strongly aligned than the distribution prior to the change in shear direction. In contrast, changing from $F_1$ to $F_4$ (rotation around the *x* axis) keeps the *a* axis distribution basically aligned with the shear direction, but with subsequent strain, the *a* axis distribution forms a girdle, decreasing the initial point-like distribution and leading to slower strain rates than prior to the change in shear direction.

#### 3.2.1.3. Shear Forces Associated With Dripping/Subduction

There are two possibilities for creating shear stress in a vertical direction as a rough approximation of the stress state associated with subduction or dripping instabilities. Changing from $F_1$ to $F_3$ (texture rotation around the *y* axis; Figure 4) results in initial deformation occurring at the same rate as for $F_1$ (because $F_1$

and $F_3$ are reciprocal deformations, as described above) followed by a decrease in strain rate (i.e., small increase in the effective viscosity) as the texture evolves (Figure 5a, cyan curve). Subsequent texture evolution produces a period with increasing strain rate, between strains of 8.5 (0.5 after the switch) to 13, peaking at $4.4 \times 10^{-14}$ s$^{-1}$. The model results exhibit a decreasing trend in strain rate immediately after this peak, reaching a final strain rate of $2 \times 10^{-14}$ s$^{-1}$ (after a total strain of 21). In contrast, changing from $F_1$ to $F_5$ (orange curve in Figure 5b) induces a dramatically diminished strain rate ($5 \times 10^{-15}$ s$^{-1}$, equivalent to that produced by $F_2$ as described above) that slowly recovers over the next 20–25 Myr (by a total strain of 14) and stabilizes around 2.2–2.3 $\times 10^{-14}$ s$^{-1}$, which is slightly higher than the strain rate at high stresses in model 1. Similar to the "transform fault" models, the strain rate curves for "subduction/dripping" can be linked to the texture development. The higher strain rate at the end of the model that applies $F_5$ ($x$ then $y$ rotation) compared to the model end after applying $F_3$ results from a more point-like distribution of the olivine $a$ axes (Figures 5a and 5b).

#### 3.2.2. Rate of Rotation of the Stress Orientation

In the preceding section, the change in texture orientation relative to the applied forces was instantaneous. In the following sections, the rate, timing, and amount of rotation of the olivine aggregate are examined. Here we focus on the simplest case, a change in the plate motion direction ($F_1$ changing to $F_2$). Here, we impose a 90° rotation over a time interval ranging from 1 to 13 Myr, after ~14 Myr of initial shearing (an accumulated strain of 8).

As described above, we use $\alpha$ and $\beta$ (Equation 9) to indicate the angle between the $x$ axis (in the aggregate reference frame) and the shear force and plate motion directions, respectively. During rotation of the aggregate, $\alpha$ linearly changes with time from 0° to −90°. In contrast, the angle $\beta$ does not change linearly with time and can differ from $\alpha$ significantly because the olivine texture excites plate motion differently in varied directions. During the rotation period, and independently of its duration, the plate movement differs from the shear direction by up to 20° (Figure 6a). Minor differences can be observed depending on the rotation rate. Once 90° rotation is achieved, the plate movement is parallel to the shear direction (1- and 10-Myr rotation period), overturned (3- and 5-Myr rotation period), or rotated less than the shear direction (13-Myr rotation period). After rotation, all models evolve in a similar manner, resulting in velocity vectors 15–20° away from the shear direction. The plate speed drastically decreases, reaching 3 cm/year by the end of the rotation period (Figure 6b). As in the instantaneous rotation model, the plate movement cannot recover its original rate after the rotation (Figure 6b). The models with shorter rotation time (1–5 Myr) reach a maximum of 7 cm/year, while the models with longer texture rotation time (10–13 Myr) reach a maximum of 5 cm/year by the end of the model (at strain ~20–21). Interestingly, during the first ~4° of rotation, the plate velocity increases, except for the model with 1-Myr rotation time, where the rotation step is 9°/time step (as the time step is fixed to 100 kyr during the rotation). This increase can be explained by the mean orientation of the olivine texture (see pole figures for a strain of 8 on Figure 3) and the plate movement (Figure 6a) before the onset of rotation, which are both a few degrees (~4° and −1.2°, respectively) offset from the shear direction. Hence, at the onset of rotation, the texture initially becomes more aligned with the shearing, resulting in up to 2 cm/year increase in the plate velocity (see texture evolution animations, which are available in the supplementary materials for each model).

#### 3.2.3. Role of Texture Evolution Prior to the Rotation

In an additional series of calculations, we varied the amount of accumulated strain between 2 and 14 prior to a 90° rotation, which was implemented using two different rotation rates (90° and 9°/Myr).

The magnitude of the velocity decrease associated with rotation appears to be proportional to the textural maturity of the aggregate before rotation (Figure 7b). However, the rate of rotation has only a small effect, as described previously (Figure 6). Note that for the models in which the rotation is imposed after a strain of 11 or 14, faster rotation results in a slightly lower minimum plate velocity (Figure 7d). Only the model with fast and early rotation (rotation at a strain of 2) exhibits velocities that return to the original plate velocity magnitude, while the other models reach strain of 21 with only 5.4–8.4 cm/year plate velocity (Figure 7b).

A large range of variation in the plate motion direction can be observed depending on the amount of initial strain, rotation rate, and time/total accumulated strain (Figures 7a and 7c). In most of the models, the difference $\alpha$-$\beta$ grows from ~−1° to ~15–20° during rotation (see the two outlined circles in each line on Figure 7c), which is also the maximum difference between $\alpha$ and $\beta$. There are three slight outlier models,

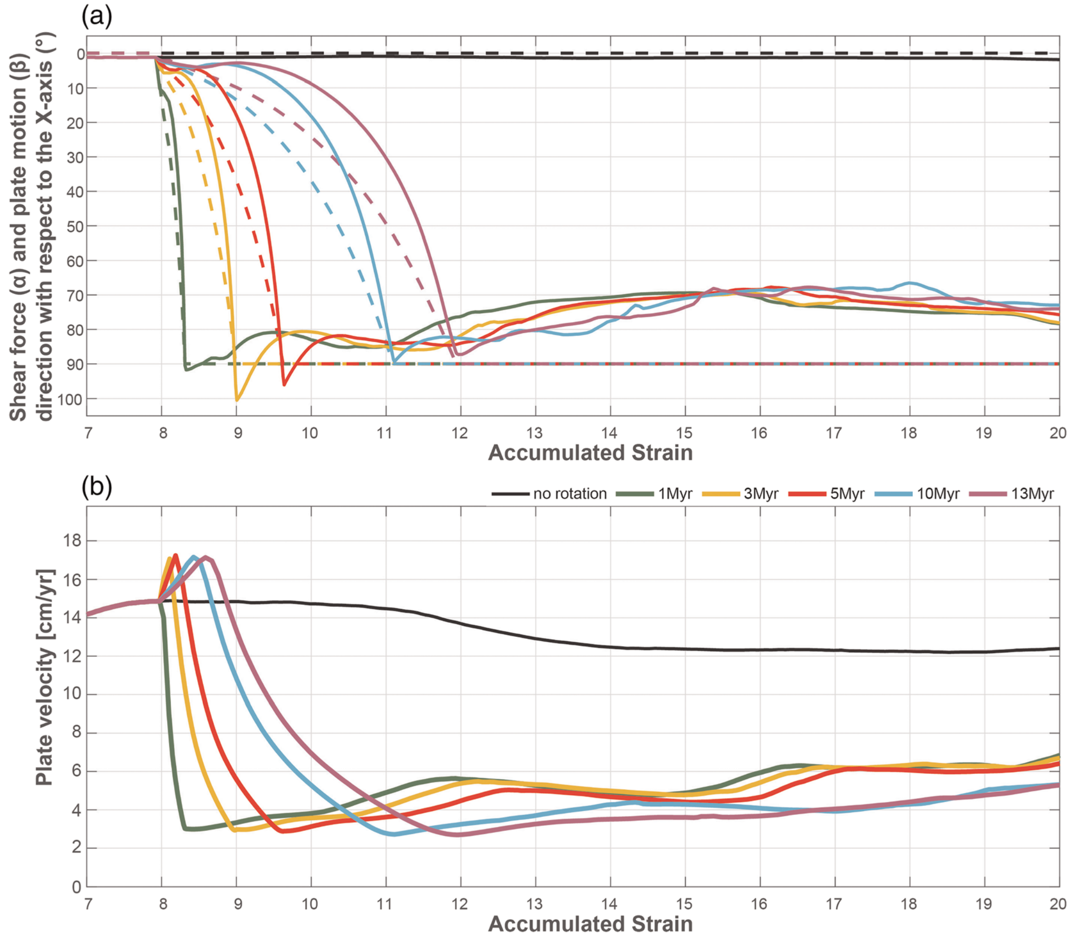


**Figure 6.** Results from models with different rates of imposed rotation of the shear stress. An initial texture (associated with an accumulated strain of 8, using model 1 of Figure 2) is rotated 90° around the $z$ axis (representing a change from $2F_1$ to $F_2$) within a period between 1 and 13 Myr. (a) Change in the direction of the shear force ($\alpha$, dashed lines) and plate motion ($\beta$, solid lines) with respect to the $x$ axis (fixed to the mantle), as a function of accumulated strain. (b) Amplitude of the plate velocity as a function of accumulated strain.

in which extreme magnitudes of $\alpha$-$\beta$ occur during the model evolution. With an initial strain of 5 and a slow-rotation rate, the plate motion direction can differ from the shear direction by up to 29°, while in the models in which an initial strain of 14 is imposed, the plate motion direction rotates more than the shear direction, reaching extremes of −6 ° and −21° (with 1- and 10-Myr rotation time, respectively).

### 3.2.4. Role of the Amount of Rotation

In more realistic geodynamic scenarios, the driving forces on plates are unlikely to rotate as much as 90°, so we additionally tested a range of rotations from 22° to 90° with slow (9°/Myr) and fast (90°/Myr) rotation rates. In all of these models, the aggregate was sheared with force $F_1$ until a strain of 8 prior to the rotation. We found (Figure 8) that the larger the rotation, the lower the average strain rate, and therefore, the lower the average plate velocity (Figures 8b and 8d). Furthermore, the models with faster rotation rates exhibit a greater variability of plate motion directions and velocities than the models with slower rotation rates (Figure 8). With only 22° rotation, $\beta$ differs from $\alpha$ by only 15° during the rotation in both models, and this difference linearly decreases as the model progresses until, at the end of the model, the plate motion becomes parallel to the shear direction. The plate velocity decreases to 7.5–7.8 cm/year, which then climbs back to the isotropic rate (~10 cm/year) by the end of the models. If the total change in shear direction is 45° or more, all models result in ~20° difference between $\alpha$ and $\beta$ during the rotation, independent of the rate of rotation. Later, the models with slower rotation rate result in even larger differences between $\alpha$ and $\beta$. The plate motion direction can change more quickly if the plate velocity is high, such as in the model with 45° rotation at 90°/Myr during

10.1029/2020GC009159

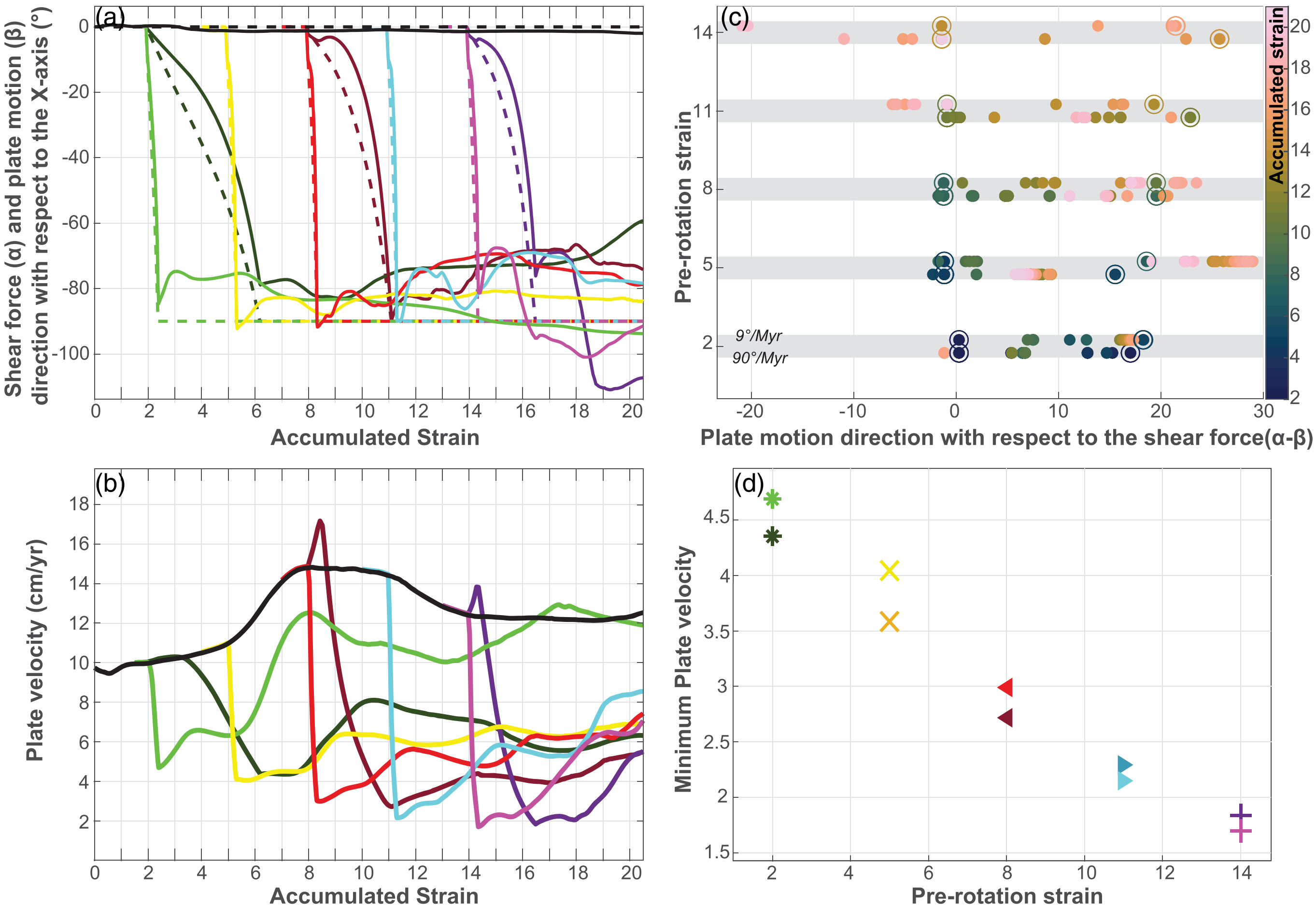


**Figure 7.** Results from models with varying amounts of accumulated strain (and therefore texture strength) at the time of the rotation (prerotation strain). (a) Direction of the shear force ($\alpha$, dashed lines) and the plate motion ($\beta$, solid lines) for models that rotate the texture 90° in either 1 Myr (lighter colors) or 10 Myr (darker colors). (b) Corresponding plate velocity amplitudes versus accumulated strain for the cases shown in (a). (c) Local minimums and maximums of the plate motion direction marked with dots that are color coded according the accumulated strain (with respect to the shear force direction) for the five tested prerotation strains. For each switch strain, upper rows represent models using the 10-Myr rotation time while the lower rows use 1-Myr rotations. (d) Minimum plate velocity (i.e., velocity right after the rotation) versus the accumulated strain after which the rotation has happened.

the period between 25 and 35 Myr (Figure 8b). On the other hand, in the model with 67° rotation at 9°/Myr, the plate velocity remains between 3.5 and 5 cm/year, and $\alpha$-$\beta$ remains ~20° (15–25°).

## 4. Discussion

The results described above suggest that the effective viscosity and strain rate of the asthenosphere, and the associated plate velocity at the surface, are extremely sensitive to the olivine texture. The asthenosphere weakens as the olivine texture develops with the $a$ axes parallel to the shear direction ("anisotropic weak" on Figure 1b), allowing for a 40% increase in plate velocity (or equally a decrease in effective viscosity). The asthenosphere acts "strong" (Figure 1c) if the mean $a$ axes direction is perpendicular to, and the mean $c$ axes direction is parallel to, the shear direction. In this case, the effective viscosity is up to ~5 times higher than if the a axes are parallel to the shear force, resulting in a slower plate velocity that is only a third of the velocity over the isotropic asthenosphere and a fifth of that in the anisotropic weak case (Figure 10). This difference in viscosity is in accordance with the differences in the strengths of the slip systems (Table 1 in Hansen, Conrad, et al., 2016), favoring deformation parallel to the $a$ axes (i.e., on the (010)[100] and (001)[100] slip systems, with strengths of 0.3 and 0.27, respectively) versus parallel to the $c$ axes (where the strength of the (010)[001] slip system is 1.29). Thus, deformations that dominantly activate the (010)[100] slip system (e.g., $F_1$ and $F_3$ at a strain of 8, Figure 5a) and the (001)[100] slip system (e.g., $F_4$ and $F_6$ at a

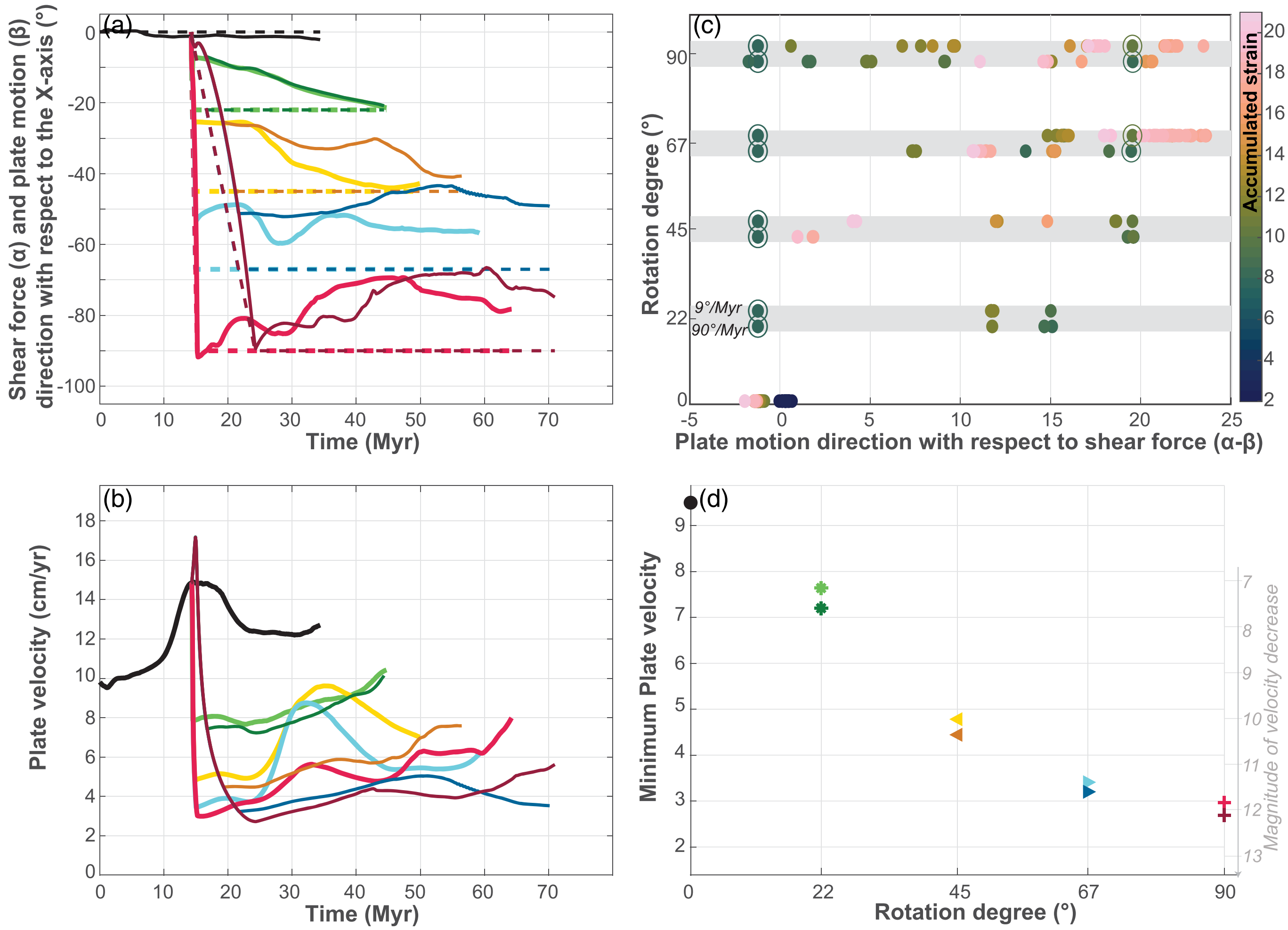


**Figure 8.** Results from models with varying amounts of rotation around the $z$ axis. (a–d) The same as in Figure 7 except using rotation angle instead of prerotation strain in (c) and (d).

strain of 8, Figure 5c) exhibit much faster strain rates compared to those that dominantly activate the (010)[001] slip system (e.g., $F_2$ and $F_5$ at a strain of 8, Figure 5b).

The evolution of the plate velocity and plate motion direction (or the entire matrix of $\dot{\varepsilon}$) is a function of the olivine texture, which evolves due to the deformation. Hence, the asthenospheric rheology depends on the kinematics and vice versa. Indeed, the models with an instantaneous change in the force direction demonstrate that applying the same stress but with different velocity boundary conditions (i.e., enforcing deformations consistent with individual forces on the asthenosphere, as shown on Figure 4) can produce very different strain rate histories (e.g., Figure 5, right column). For example, after creating a texture by force $F_1$, switching to $F_2$ or $F_5$ both involves the same new stress state and both initially activates the same (010)[001] slip system. Thus, both deformations initially produce the same (although much reduced) strain rate (Figure 5b). However, enforcing shear deformation in the vertical direction (i.e., by $F_5$) allows for faster rotations of the olivine grains into the new shear direction, allowing for higher strain rates as the texture develops.

Without changes in the shear force direction, the plate velocity evolution follows a similar trend to the values of *P-a* (point-like distribution value for the olivine *a* axes) (Figure 3). However, if the direction of the shear force changes, this correlation is less clear. We calculated the texture parameters described in section 3.1.1 for each model for a 0.5 strain increment, for which an example is presented in Figure 9. If the texture is rotated 90° around the $z$ axis with respect to the shear stress (in 1 Myr), then the changes in the values of *P-a* are no longer correlated to the changes in the plate velocity, especially around the time of the rotation

10.1029/2020GC009159

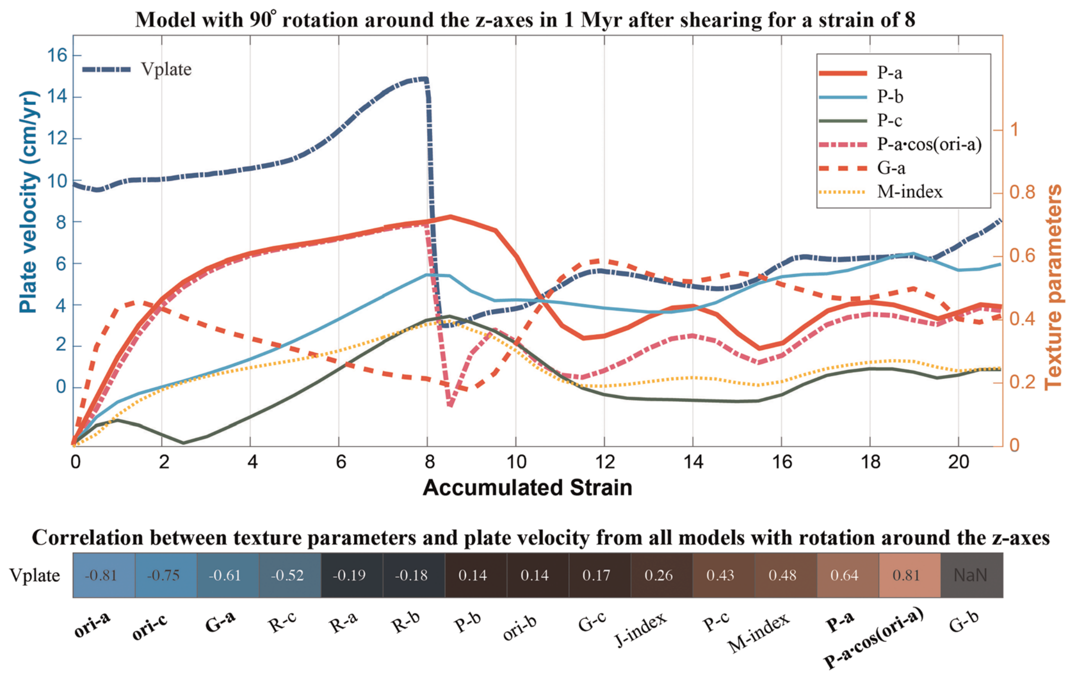


**Figure 9.** (top) Plate velocity and texture parameters, as a function of accumulated strain, for a model in which a 90° rotation (representing a change from $F_1$ to $F_2$) is imposed over 1 Myr after a strain of 8 (the fastest rotation presented in Figure 6). (bottom) Correlation between texture parameters and plate velocity based on all models with rotation (0–90°) around the $z$ axis, listed in order from negative (blue shades) to positive (red shades) correlations. Abbreviations: $v_{plate}$ = plate velocity; *ori-a* (−b; −c) = mean orientation of the olivine $a$ axes ($b$ axes; $c$ axes); $G$, $R$, $P$ (−a −b; −c) = girdle, random, and point parameters for each axis distribution, respectively (Vollmer, 1990).

(between a strain of 8 and a strain of 11), at which point the values of $P$ for the $a$, $b$, and $c$ axes (*P-a*, *P-b*, and *P-c*) and the $M$ index are the largest (Figure 9), while the plate velocity is the lowest.

To analyze the overall relationship between texture parameters and kinematic parameters (e.g., plate velocity), we performed a Pearce correlation for all the models representing shearing by plate pull. The correlation values between the plate velocity and texture parameters (Figure 9) demonstrate that the mean orientation of the olivine $a$ axes (*ori-a* on Figure 9) and the mean orientation of the $c$ axes (*ori-c*) are highly anticorrelated with the plate velocity. In contrast, *P-a* has the highest correlation with the plate velocity of 0.64, which is similar to the strength of the anticorrelation between the $G$ value (girdle-like distribution) of the $a$ axes (*G-a*) and the plate velocity ($v_{plate}$). It is important to note that these parameters are not independent from each other, as *G-a* and *P-a* are anticorrelated with a coefficient of −0.94 (similarly −0.83 between *G-b* and *P-b*) and a 0.85 correlation between *ori-a* and *ori-c* (supporting information Figure S1). Based on the correlation between the texture parameters and the plate velocity, as well as between each pair of texture parameters, we find that the plate velocity can be linked essentially to two parameters, the mean orientation and the value of $P$ for the distribution of the $a$ axes of the olivine grains, and therefore, we see the strongest correlation between the plate velocity and the product of those two parameters ($P\text{-}a \cdot \cos(ori\text{-}a)$ in Figure 9).

The need to consider both mean orientation and value of $P$ for the $a$ axes provides important context for comparison to previous investigations of texture evolution in olivine. Boneh et al. (2015) used DRex, a different model of texture evolution (Kaminski & Ribe, 2002), to investigate the influence of changing the deformation kinematics on texture. By examining scenarios similar to our cases $F_2$ and $F_3$, Boneh et al. (2015) concluded that olivine texture evolves to a new steady state by a shear strain of ~4. This conclusion was based on tracking the dominant $a$ axis orientation and is consistent with our observations (Figure 5). However, our investigation of the mechanical response of an olivine aggregate suggests that the evolution of the viscosity can be considerably more protracted (especially for $F_2$), and our correlation analysis demonstrates that additional features of the texture, most notably *P-a*, are likely responsible for that difference.

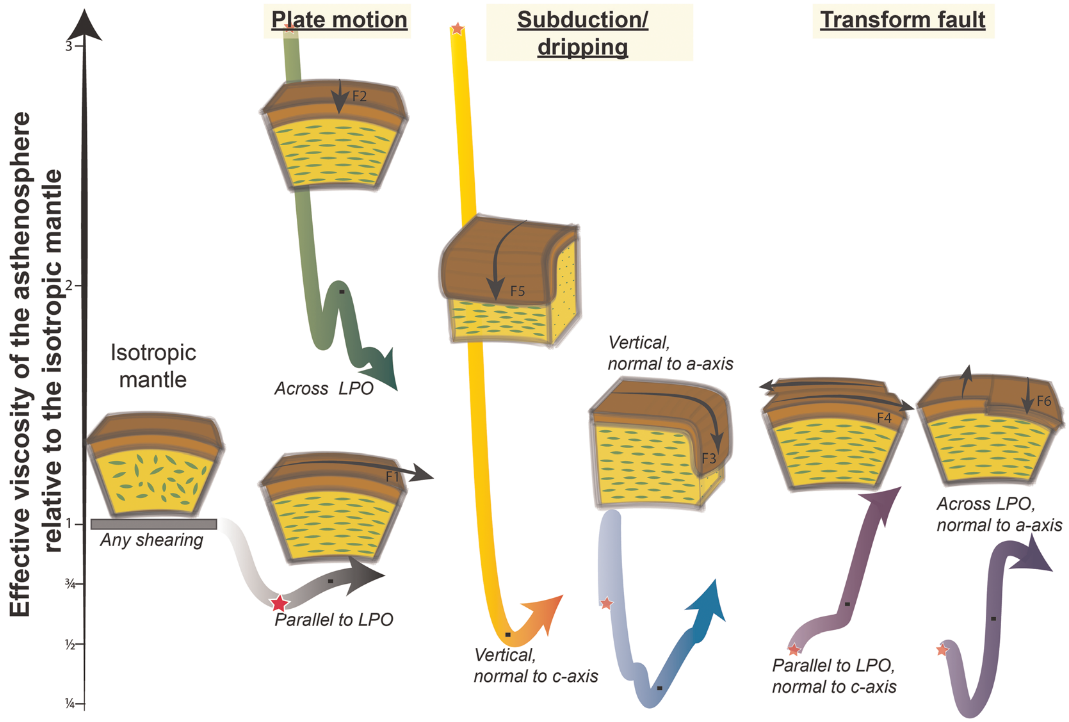


**Figure 10.** Trends for the manner in which anisotropic viscosity in the asthenosphere should influence different geodynamic situations. The white to black arrow indicates the mantle weakening path associated with development of an LPO as the asthenosphere accumulates strain due to simple shear (e.g., in model 1). The colored arrows indicate the time evolution of the relative effective viscosity (vertical dimension, values based on results shown in Figure 5) from the moment of switching the shear direction (strain of 8, marked with a star) through an accumulated strain of 14 (postrotation strain of 6, black squares) and until a strain of 21 (postrotation strain of 13, indicated by the arrow tips). Geodynamic processes for which the effective viscosity increases ($F_2$ plate motion and $F_5$ subduction/dripping) could be initially impeded by anisotropic viscosity, while those for which the effective viscosity decreases ($F_3$—subduction and dripping and $F_4$ and $F_5$—transform fault) could be initially promoted. Subsequent changes to the effective viscosity along each path indicate how continued texture development should either speed or slow each process as it develops.

The orientation of the olivine grains also exerts an important control on the direction of the plate motion (or asthenospheric flow) with respect to the driving force. As noted above, in the case of continuous shearing in one direction, the shear stress induces very little nonparallel shear strain, but as soon as the shear direction is changed toward the mean orientation of the olivine *c* axes (i.e., the strongest slip system), we observe an increase in strain rates in directions that are nonparallel to the shear stress. While the relationship between these factors is not straightforward, it is clear that as *ori-a* starts to differ from the shear direction, there is a corresponding change in the plate motion direction (Figures 7 and 8). The highest values of $\beta$ (plate motion direction) occur at times in which *ori-a* differs 30–60° from the shear direction. When this angle is higher, $\beta$ decreases to ~0°, and the plate velocity slows considerably. This behavior occurs because it is not possible to create strain perpendicular to the forcing. Thus, when a grain is oriented such that the *a* axis is perpendicular to the shear direction, the easiest slip system cannot be activated (supporting information Figure S2).

## 5. Relevance to Natural Phenomena

Although our models are simplistic by nature, we can use them to gain some intuition about how viscous anisotropy may affect different geodynamic processes. However, before we proceed, it is important to note the limitations of our models. In particular, we have assumed that the asthenosphere under a large (6,000 × 6,000 km$^2$) plate deforms uniformly, and therefore, the olivine texture, and its associated rheology, changes uniformly under the entire plate. Certainly, we may expect some textural heterogeneity for most realistic geodynamic scenarios, and this complexity may localize or otherwise change deformation patterns, affecting the results. Furthermore, our assumption that deformation occurs in a 200 km thick homogeneous layer of asthenosphere does not account for the possibility that deformation may be shifted to deeper layers if asthenospheric textures act to increase the asthenosphere's effective viscosity. Indeed, such a scenario is consistent with layered anisotropic textures under continents (e.g., Yuan & Romanowicz, 2010) and oceans (e.g., Beghein et al., 2014). Furthermore, other factors not included in our model, such as the presence of melt or strain localization, may affect deformation and/or textural development. As an example, our model also does not explicitly account for dynamic recrystallization, which Signorelli and Tommasi (2015) showed can slightly increase the rate of fabric realignment relative to models with no recrystallization. However, our model parameters are calibrated based on laboratory experiments that inherently include such recrystallization (Hansen, Conrad, et al., 2016; Hansen, Warren, et al., 2016), and therefore, any application of this model assumes that rates of dynamic recrystallization are similar to those in laboratory experiments.

Despite these caveats, our simple experiments suggest that the textural anisotropy of the mantle should be associated with directional differences in effective viscosity that can be large (up to order of magnitude) and can change with time as textures develop. Anisotropic viscosity should thus influence a range of different geodynamic processes, and we can use our simple models to identify these influences (Figure 10). In particular, depending on the orientation of the tectonic force with respect to the mean orientation of the olivine grains, and with respect to the three slip systems that can accommodate deformation, the anisotropic texture may either assist or resist continued deformation for a given process. This means that anisotropic viscosity may facilitate certain types of tectonic processes and impede others. We can thus use our simple models to generally characterize the expected trends relating viscous anisotropy to geodynamic processes. More quantitative characterization of the impact of viscous anisotropy will require more sophisticated modeling efforts.

### 5.1. Change in the Direction of Plate Motion

By changing the orientation of the shear force in the horizontal direction (e.g., Figure 5a), we demonstrate that the asthenospheric texture should significantly influence the motion of a tectonic plate. Indeed, for horizontally oriented shear, the effective viscosity of an olivine aggregate may be a factor of ~5 times smaller when the shear force is parallel to the mean orientation of the *a* axis of olivine grains (*ori-a*) compared to perpendicular to *ori-a* (Figure 10). Thus, if the texture beneath the plate is characterized by strong alignment of the *a* axes, then a large change in the orientation of forces on the plate may result in a significant slowing of the plate velocity (up to a factor of 5 in the case of a uniformly deforming asthenosphere), even if the change in the orientation of forces occurs over a period of more than 10 Myr (Figure 6). The stronger the initial texture (e.g., formed as a result of strains greater than 2, Figure 7) and the larger the change in the orientation of the plate driving force (e.g., more than 45°, Figure 8), the larger and more lasting the asthenospheric resistance will be to changes in the orientation of the driving forces. This asthenospheric resistance, induced by shear forces misaligned with the preferred orientation of the texture, can also result in plate motion that is not parallel to the plate driving force (Figures 6a, 7a, and 8a). This misalignment can last for tens of millions of years because the asthenospheric texture may be slow to redevelop.

Thus, we expect that anisotropic viscosity may significantly modify the relationship between plate motions and the forces that drive them (e.g., Becker et al., 2006; Conrad & Lithgow-Bertelloni, 2004). Although Becker and Kawakatsu (2011) found that mantle flow models that included viscosity anisotropy behaved similarly to isotropic models, their study did not examine time-dependent behavior. Instead, our results suggest that time-dependent changes to the driving forces on plates, or to the amplitude or orientation of the anisotropic texture beneath them, should result in potentially large differences between the orientation of the net driving force on a plate and the direction of the resulting asthenospheric flow and plate motion. Note that the effective viscosity of the asthenosphere may also vary spatially beneath the plate depending on the orientation and maturity of the olivine texture locally. These spatial, temporal, and directional differences in the resistance that the asthenosphere exerts on plate motions may persist for durations of tens of million years (e.g., Figure 8).

Our results suggest that anisotropic viscosity may cause a plate to respond only sluggishly to changes in the direction of its driving forces. Indeed, plate motions in global plate reconstruction models are observed to remain relatively stable for long periods (tens of millions of years), except for a few brief periods of global reorganization (Bercovici et al., 2000). This overall stability has been attributed to slow evolution of the plate driving forces (e.g., Richards & Lithgow-Bertelloni, 1996), despite the possibility that slab breakoff (Andrews & Billen, 2009) or even a change in the direction and magnitude of subduction-related stresses (e.g., Capitanio et al., 2011; Jahren et al., 2005) may change the driving forces on plates quickly. The

10.1029/2020GC009159

sluggishness with which anisotropic textures adjust to changes in the orientation of the applied driving force may represent an alternative mechanism to explain the gradual changes in the direction of plate motions observed in reconstructions. This mechanism predicts that driving forces, asthenospheric resistance, and hence plate motions may be misaligned for significant periods of time. Indeed such misalignment might be relevant for the Pacific plate over the past 20 Myr (Faccenna et al., 2012).

### 5.2. Transform Faults

Asthenospheric mantle, sheared by plate motions, should experience shear stresses in a horizontal direction on vertical planes near transform faults. Strain that results from these stresses will be enhanced by viscous anisotropy. If the shearing direction is parallel to the plate motions that generated the asthenospheric texture ($F_4$ in Figures 4, 5c, and 10), the initially weakened asthenosphere will likely become stronger due to the evolving texture that results in a strengthening, girdle-like distribution. For transform motion perpendicular to this texture ($F_6$ in Figures 4, 5c, and 10), the initial rotation of the olivine grains significantly weakens the asthenosphere. Interestingly, the results of this simple analysis are consistent with the large number of transform faults in the oceanic lithosphere. Although transform faults usually form close to the ridge where the asthenosphere has not been sheared for long, and where texture development involves a more complicated history associated with corner flow (Blackman et al., 2017), it is possible that the low asthenospheric resistance aids the formation of lithospheric scale transform faults.

### 5.3. Initiation of Subduction or Dripping

Changing the direction of the shear force from horizontal to vertical can be roughly associated with the initiation of slab subduction or dripping of lithospheric mantle. Our results ($F_3$ and $F_5$ in Figures 5a, 5b, and 10) suggest that asthenosphere with well-oriented olivine grains imposes small resistance for such processes if they are oriented perpendicular to the initial plate motion direction, but large resistance if they are oriented on the plane that is parallel to the plate motion. This finding is consistent with the observed orientation of subduction trenches, which are usually close to perpendicular to the long-term plate motion direction. Motion in response to a vertically oriented shear force on a plane perpendicular to the initial plate motion direction (e.g., trench-perpendicular subduction, $F_3$ in Figure 4) exhibits a short period of increased resistance to deformation that must be overcome before the texture weakens (Figure 5c, blue curve). Thus, asthenospheric textures may initially pose a slight impediment to subduction initiation, but after a few million years, the olivine texture evolution may hasten the evolution of subduction. In contrast, vertical motion in response to a vertical shear force on a plane parallel to plate motions (e.g., very oblique subduction or Richter rolls, $F_1$ to $F_5$ in Figure 4) is highly resisted by the anisotropic fabric, but in the long term, olivine texture development induces asthenospheric weakening, which may allow for accelerated growth of lithospheric instabilities (Figure 5b, orange curve).

However, both subduction initiation and small-scale convection involve more complex deformation than the simple instantaneous change in shear direction that is modeled here. For example, subduction zones often start along transform faults or in the vicinity of active subductions (Crameri et al., 2020), both of which can fundamentally change the asthenospheric texture and hence its resistance to the formation of new slabs or lithospheric instabilities. The rheology of the lithosphere also plays a potentially large role in subduction initiation, and it is possible that olivine texture can become frozen into the oceanic lithosphere as it cools (Tommasi, 1998), which would likely affect the rheology of the plate, and hence its resistance to bending. Although analysis of this deformation is beyond the scope of this study, the combined effect of asthenospheric and lithospheric weakening due to anisotropy could allow for subduction zone initiation in response to lower tectonic stresses than usually expected (e.g., Gurnis et al., 2004). To explore the role of asthenospheric and lithospheric viscous anisotropy in such complex processes, more sophisticated 3-D geodynamic modeling is required.

## 6. Conclusions

Olivine texture development in the asthenosphere and its response to shearing are highly coupled and can exert considerable influences on geodynamic processes. In response to unidirectional shearing of the asthenosphere, the formation of an olivine texture causes a significant decrease in effective mantle viscosity after accumulating a shear strain of ~5. After this texture has formed, changes to the direction of the forces on the system, as induced by a change in the tectonic setting, result in a different effective viscosity because of the mechanically anisotropic nature of the textured asthenosphere. Our results indicate that differences in the effective viscosity associated with shearing asthenosphere primarily result from the relative activation of olivine's weak and strong slip systems. The resulting differences in effective viscosity can be over an order of magnitude and should hinder some tectonic processes and foster others, depending on their sense of deformation relative to asthenospheric textures (Figure 10). If the new shear direction is such that the strongest slip system, (010)[001], has to be activated to produce deformation, then the effective viscosity will increase. This increase is generally the case for a change in the direction of plate motion or vertical shearing on a plane parallel to plate motions. In contrast, the mantle should remain weak, or even become weaker, for shear forces that primarily induce deformation on the other two, weaker slip systems, (010)[100] and (001)[100], which is the case for transform motions, subduction initiation, or ongoing plate motion in the same direction. Thus, based on our simple models, we expect asthenospheric textures to significantly slow changes to the direction of plate motions and hinder the formation of ridge-perpendicular subduction zones. Conversely, these textures should assist in the initiation of new subduction zones parallel to mid-ocean ridges (perpendicular to plate motion) and promote the development of lithospheric scale transform faults. To fully understand the impact of anisotropic viscosity on plate tectonics and asthenospheric dynamics, olivine texture development, and the anisotropic viscosity that is associated with it, needs to be integrated into 3-D dynamic models of the relevant processes.

## Data Availability Statement

Data and code availability (https://doi.org/10.11582/2020.00039) (Please also refer to the supporting information for more information about the model data and code.).

**Acknowledgments**
This manuscript was significantly improved by constructive feedback from two anonymous reviewers. This work was supported by the Research Council of Norway Centres of Excellence project 223272.

## References

Andrews, E. R., & Billen, M. I. (2009). Rheologic controls on the dynamics of slab detachment. *Tectonophysics*, *464*(1–4), 60–69. https://doi.org/10.1016/j.tecto.2007.09.004

Bamford, D., & Crampin, S. (1977). Seismic anisotropy—The state of the art. *Geophysical Journal of the Royal Astronomical Society*, *49*(1), 1–8. https://doi.org/10.1111/j.1365-246X.1977.tb03697.x

Becker, T. W. (2008). Azimuthal seismic anisotropy constrains net rotation of the lithosphere. *Geophysical Research Letters*, *35*, L05303. https://doi.org/10.1029/2007GL032928

Becker, T. W., Chevrot, S., Schulte-Pelkum, V., & Blackman, D. K. (2006). Statistical properties of seismic anisotropy predicted by upper mantle geodynamic models. *Journal of Geophysical Research*, *111*(B8), 111. https://doi.org/10.1029/2005JB004095

Becker, T. W., Conrad, C. P., Schaeffer, A. J., & Lebedev, S. (2014). Origin of azimuthal seismic anisotropy in oceanic plates and mantle. *Earth and Planetary Science Letters*, *401*, 236–250. https://doi.org/10.1016/j.epsl.2014.06.014

Becker, T. W., & Kawakatsu, H. (2011). On the role of anisotropic viscosity for plate-scale flow. *Geophysical Research Letters*, *38*, n/a. https://doi.org/10.1029/2011GL048584

Becker, T. W., Kellogg, J. B., Ekström, G., & O'Connell, R. J. (2003). Comparison of azimuthal seismic anisotropy from surface waves and finite strain from global mantle-circulation models. *Geophysical Journal International*, *155*(2), 696–714. https://doi.org/10.1046/j.1365-246X.2003.02085.x

Becker, T. W., Kustowski, B., & Ekström, G. (2008). Radial seismic anisotropy as a constraint for upper mantle rheology. *Earth and Planetary Science Letters*, *267*(1–2), 213–227. https://doi.org/10.1016/j.epsl.2007.11.038

Beghein, C., Yuan, K., Schmerr, N., & Xing, Z. (2014). Changes in seismic anisotropy shed light on the nature of the Gutenberg discontinuity. *Science*, *343*(6176), 1237–1240. https://doi.org/10.1126/science.1246724

Behn, M. D., Conrad, C. P., & Silver, P. G. (2004). Detection of upper mantle flow associated with the African Superplume. *Earth and Planetary Science Letters*, *224*(3–4), 259–274. https://doi.org/10.1016/j.epsl.2004.05.026

Bercovici, D., Ricard, Y., & Richards, M. A. (2000). The relation between mantle dynamics and plate tectonics: A primer. In M. A. Richards, R. G. Gordon, & R. D. van der Hilst (Eds.), *Geophysical Monograph Series* (pp. 5–46). Washington, D. C.: American Geophysical Union. https://doi.org/10.1029/GM121p0005

Blackman, D. K., Boyce, D. E., Castelnau, O., Dawson, P. R., & Laske, G. (2017). Effects of crystal preferred orientation on upper-mantle flow near plate boundaries: Rheologic feedbacks and seismic anisotropy. *Geophysical Journal International*, *210*(3), 1481–1493. https://doi.org/10.1093/gji/ggx251

Boneh, Y., Morales, L. F. G., Kaminski, E., & Skemer, P. (2015). Modeling olivine CPO evolution with complex deformation histories: Implications for the interpretation of seismic anisotropy in the mantle. *Geochemistry, Geophysics, Geosystems*, *16*, 3436–3455. https://doi.org/10.1002/2015GC005964

Bunge, H. (1982). *Texture Analysis in Materials Science: Mathematical Models*. London: Butterworths.

Capitanio, F. A., Faccenna, C., Zlotnik, S., & Stegman, D. R. (2011). Subduction dynamics and the origin of Andean orogeny and the Bolivian orocline. *Nature*, *480*(7375), 83–86. https://doi.org/10.1038/nature10596

Christensen, N. I. (1984). The magnitude, symmetry and origin of upper mantle anisotropy based on fabric analyses of ultramafic tectonites. *Geophysical Journal International*, *76*(1), 89–111. https://doi.org/10.1111/j.1365-246X.1984.tb05025.x

Christensen, U. R. (1987). Some geodynamical effects of anisotropic viscosity. *Geophysical Journal of the Royal Astronomical Society*, *91*(3), 711–736. https://doi.org/10.1111/j.1365-246X.1987.tb01666.x

Conrad, C. P., & Behn, M. D. (2010). Constraints on lithosphere net rotation and asthenospheric viscosity from global mantle flow models and seismic anisotropy. *Geochemistry, Geophysics, Geosystems 11*, Q05W05. https://doi.org/10.1029/2009GC002970

Conrad, C. P., & Lithgow-Bertelloni, C. (2004). The temporal evolution of plate driving forces: Importance of "slab suction" versus "slab pull" during the Cenozoic. *Journal of Geophysical Research B*, *109*(B10), 1–14. https://doi.org/10.1029/2004JB002991

Crameri, F., Magni, V., Domeier, M., Shephard, G. E., Chotalia, K., Cooper, G., et al. (2020). A transdisciplinary and community-driven database to unravel subduction zone initiation. *Nature Communications*, *11*(1), 3750. https://doi.org/10.1038/s41467-020-17522-9

Dellinger, J., Vasicek, D., & Sondergeld, C. (1998). Kelvin notation for stabilizing elastic-constant inversion. *Revue de l'Institut Français du Pétrole*, *53*(5), 709–719. https://doi.org/10.2516/ogst:1998063

Durham, W. B., & Goetze, C. (1977). Plastic flow of oriented single crystals of olivine: 1. Mechanical Data. *Journal of Geophysical Research*, *82*(36), 5737–5753. https://doi.org/10.1029/JB082i036p05737

Eakin, C. M., Rychert, C. A., & Harmon, N. (2018). The role of oceanic transform faults in seafloor spreading: A global perspective from seismic anisotropy. *Journal of Geophysical Research: Solid Earth*, *123*, 1736–1751. https://doi.org/10.1002/2017JB015176

Faccenna, C., Becker, T. W., Lallemand, S., & Steinberger, B. (2012). On the role of slab pull in the Cenozoic motion of the Pacific plate. *Geophysical Research Letters*, *39*, L03305. https://doi.org/10.1029/2011GL050155

Gaboret, C., Forte, A. M., Montagner, J.-P. (2003). The unique dynamics of the Pacific hemisphere mantle and its signature on seismic anisotropy. *Earth and Planetary Science Letters 208*, 219–233. https://doi.org/10.1016/S0012-821X(03)00037-2, 3–4

Gurnis, M., Hall, C., & Lavier, L. (2004). Evolving force balance during incipient subduction. *Geochemistry, Geophysics, Geosystems*, *5*, Q07001. https://doi.org/10.1029/2003GC000681

Hansen, L. N., Conrad, C. P., Boneh, Y., Skemer, P., Warren, J. M., & Kohlstedt, D. L. (2016). Viscous anisotropy of textured olivine aggregates: 2. Micromechanical model. *Journal of Geophysical Research: Solid Earth*, *121*, 7965–7983. https://doi.org/10.1002/2016JB013304

Hansen, L. N., Warren, J. M., Zimmerman, M. E., & Kohlstedt, D. L. (2016). Viscous anisotropy of textured olivine aggregates, Part 1: Measurement of the magnitude and evolution of anisotropy. *Earth and Planetary Science Letters*, *445*, 92–103. https://doi.org/10.1016/j.epsl.2016.04.008

Hansen, L. N., Zimmerman, M. E., & Kohlstedt, D. L. (2012). Laboratory measurements of the viscous anisotropy of olivine aggregates. *Nature*, *492*(7429), 415–418. https://doi.org/10.1038/nature11671

Jahren, A. H., Conrad, C. P., Arens, N. C., Mora, G., & Lithgow-Bertelloni, C. (2005). A plate tectonic mechanism for methane hydrate release along subduction zones. *Earth and Planetary Science Letters*, *236*(3–4), 691–704. https://doi.org/10.1016/j.epsl.2005.06.009

Kaminski, É., & Ribe, N. M. (2002). Timescales for the evolution of seismic anisotropy in mantle flow. *Geochemistry, Geophysics, Geosystems*, *3*(8). https://doi.org/10.1029/2001GC000222

Karato, S. (1987). Seismic anisotropy due to lattice preferred orientation of minerals: Kinematic or dynamic? In M. H. Manghnani, & Y. Syono (Eds.), *Geophysical Monograph Series* (pp. 455–471). Washington, D. C.: American Geophysical Union. https://doi.org/10.1029/GM039p0455

Karato, S., & Wu, P. (1993). Rheology of the upper mantle: A synthesis. *Science*, *260*(5109), 771–778. https://doi.org/10.1126/science.260.5109.771

Lev, E., & Hager, B. H. (2008). Rayleigh-Taylor instabilities with anisotropic lithospheric viscosity. *Geophysical Journal International*, *173*(3), 806–814. https://doi.org/10.1111/j.1365-246X.2008.03731.x

Lev, E., & Hager, B. H. (2011). Anisotropic viscosity changes subduction zone thermal structure. *Geochemistry, Geophysics, Geosystems*, *12*, n/a. https://doi.org/10.1029/2010GC003382

Long, M. D. (2013). Constraints on Subduction geodynamics from seismic anisotropy. *Reviews of Geophysics*, *51*, 76–112. https://doi.org/10.1002/rog.20008

Long, M. D., & Becker, T. W. (2010). Mantle dynamics and seismic anisotropy. *Earth and Planetary Science Letters*, *297*, 341–354. https://doi.org/10.1016/j.epsl.2010.06.036

Mainprice, D., Bachmann, F., Hielscher, R., & Schaeben, H. (2015). Descriptive tools for the analysis of texture projects with large datasets using MTEX: Strength, symmetry and components. *Geological Society, London, Special Publications*, *409*(1), 251–271. https://doi.org/10.1144/SP409.8

Mühlhaus, H.-B., Čada, M., & Moresi, L. (2003). Anisotropic convection model for the Earth's mantle. In P. M. A. Sloot, D. Abramson, A. V. Bogdanov, Y. E. Gorbachev, J. J. Dongarra, & A. Y. Zomaya (Eds.), *Computational Science—ICCS 2003* (pp. 788–797). Berlin Heidelberg, Berlin, Heidelberg: Springer. https://doi.org/10.1007/3-540-44863-2_77

Mühlhaus, H.-B., Moresi, L., Hobbs, B., & Dufour, F. (2002). Large amplitude folding in finely layered viscoelastic rock structures. *Pure and Applied Geophysics*, *159*(10), 2311–2333. https://doi.org/10.1007/s00024-002-8737-4

Pouilloux, L., Kaminski, E., & Labrosse, S. (2007). Anisotropic rheology of a cubic medium and implications for geological materials. *Geophysical Journal International*, *170*(2), 876–885. https://doi.org/10.1111/j.1365-246X.2007.03461.x

Ribe, N. M. (1989). Seismic anisotropy and mantle flow. *Journal of Geophysical Research: Solid Earth*, *94*(B4), 4213–4223.

Richards, M. A., Lithgow-Bertelloni, C. (1996). Plate motion changes, the Hawaiian-emperor bend, and the apparent success and failure of geodynamic models. *Earth and Planetary Science Letters 137*, 19–27. https://doi.org/10.1016/0012-821X(95)00209-U, 1–4

Schellart, W. P. (2004). Kinematics of subduction and subduction-induced flow in the upper mantle. *Journal of Geophysical Research B*, *109*(B7), 1–19. https://doi.org/10.1029/2004JB002970

Signorelli, J., & Tommasi, A. (2015). Modeling the effect of subgrain rotation recrystallization on the evolution of olivine crystal preferred orientations in simple shear. *Earth and Planetary Science Letters*, *430*, 356–366. https://doi.org/10.1016/j.epsl.2015.08.018

Silver, P. G. (1996). Seismic anistropy beneath the continents: Probing the depths of geology. *Annual Review of Earth and Planetary Sciences*, *24*(1), 385–432. https://doi.org/10.1146/annurev.earth.24.1.385

Skemer, P., Katayama, I., Jiang, Z., & Karato, S. (2005). The misorientation index: Development of a new method for calculating the strength of lattice-preferred orientation. *Tectonophysics*, *411*(1–4), 157–167. https://doi.org/10.1016/j.tecto.2005.08.023

Stixrude, L., & Lithgow-Bertelloni, C. (2005). Mineralogy and elasticity of the oceanic upper mantle: Origin of the low-velocity zone. *Journal of Geophysical Research*, *110*, B03204. https://doi.org/10.1029/2004JB002965

Tanimoto, T., & Anderson, D. L. (1984). Mapping convection in the mantle. *Geophysical Research Letters*, *11*(4), 287–290. https://doi.org/10.1029/GL011i004p00287

Taylor, G. I. (1938). Plastic strain in metals. *Journal of the Institute of Metals*, *62*.

Tommasi, A. (1998). Forward modeling of the development of seismic anisotropy in the upper mantle. *Earth and Planetary Science Letters 160*, 1–13. https://doi.org/10.1016/S0012-821X(98)00081-8, 1–2

Vollmer, F. W. (1990). An application of eigenvalue methods to structural domain analysis. *Bulletin of the Geological Society of America*, *102*(6), 786–791. https://doi.org/10.1130/0016-7606(1990)102<0786:AAOEMT>2.3.CO;2

Yuan, H., & Romanowicz, B. (2010). Lithospheric layering in the North American craton. *Nature*, *466*(7310), 1063–1068. https://doi.org/10.1038/nature09332